LAWRENCE
LIVERMORE
NATIONAL
LABORATORY

LLNL-JRNL-419883

Ground motion modeling of Hayward fault scenario earthquakes II:Simulation of long-period and broadband ground motions

Brad T. Aagaard, Robert W. Graves, Arthur Rodgers, Thomas M. Brocher, Robert W. Simpson, Douglas Dreger, N. Anders Petersson, Shawn C. Larsen, Shuo Ma, Robert C. Jachens

November 10, 2009

The Bulletin of the Seismological Society of America

Disclaimer

Ground motion modeling of Hayward fault scenario earthquakes II: Simulation of long-period and broadband ground motions

by Brad T. Aagaard, Robert W. Graves, Arthur Rodgers, Thomas M. Brocher, Robert W. Simpson, Douglas Dreger, N. Anders Petersson, Shawn C. Larsen, Shuo Ma, and Robert C. Jachens

November 2, 2009

For submission to BSSA

The electronic supplement is available at http://www.sf06simulation.org/supplement/hayward_gmsims/.

Abstract We simulate long-period (T $>$ 1.0–2.0 s) and broadband (T $>$ 0.1 s) ground motions for 39 scenarios earthquakes (Mw 6.7–7.2) involving the Hayward, Calaveras, and Rodgers Creek faults. For rupture on the Hayward fault we consider the effects of creep on coseismic slip using two different approaches, both of which reduce the ground motions compared with neglecting the influence of creep. Nevertheless, the scenario earthquakes generate strong shaking throughout the San Francisco Bay area with about 50% of the urban area experiencing MMI VII or greater for the magnitude 7.0 scenario events. Long-period simulations of the 2007 Mw 4.18 Oakland and 2007 Mw 4.5 Alum Rock earthquakes show that the USGS Bay Area Velocity Model version 08.3.0 permits simulation of the amplitude and duration of shaking throughout the San Francisco Bay area, with the greatest accuracy in the Santa Clara Valley (San Jose area). The ground motions exhibit a strong sensitivity to the rupture length (or magnitude), hypocenter (or rupture directivity), and slip distribution. The ground motions display a much weaker sensitivity to the rise time and rupture speed. Peak velocities, peak accelerations, and spectral accelerations from the synthetic broadband ground motions are, on average, slightly higher than the Next Generation Attenuation (NGA) ground-motion prediction equations. We attribute at least some of this difference to the relatively narrow width of the Hayward fault ruptures. The simulations suggest that the Spudich and Chiou (2008) directivity corrections to the NGA relations could be improved by including a dependence on the rupture speed and increasing the areal extent of rupture directivity with period. The simulations also indicate that the NGA relations may under-predict amplification in shallow sedimentary basins.

Introduction

In Part I (Aagaard *et al*., XXXX) we discussed the construction of a suite of 39 earthquake scenarios involving rupture of the Hayward fault. Some of the scenarios also involve rupture of a 23 km portion of the Calaveras fault (six scenarios) or rupture of the Rodgers Creek fault (four scenarios). The scenarios are designed to permit analysis of the ground motions for a wide variety of plausible ruptures on the Hayward-Rodgers Creek fault system, which carries the highest probability of producing a magnitude 6.7 or larger event in the next 30 years (WGCEP, 2008). The most recent large rupture of the Hayward fault, a magnitude 6.8 event (Bakun, 1999), occurred on 21 October 1868 and caused widespread damage throughout the sparsely populated eastern side of the San Francisco Bay and significant damage in the city of San Francisco (Boatwright and Bundock, 2008). Moreover, as a result of the level of damage in San Francisco, the 1868 earthquake was called the "Great San Francisco Earthquake" until the 18 April 1906 magnitude 7.9 earthquake (Stover and Coffman, 1993).

In previous work we estimated ground motions for the 1906 earthquake and scenarios rupturing that same 480 km portion of the northern San Andreas fault (Aagaard *et al*., 2008a) as well as the 1989 magnitude 6.9 Loma Prieta earthquake (Aagaard *et al*., 2008b). The simulations demonstrated consistent amplification of shaking associated with sedimentary basins, such as such as the Cupertino Basin west of San Jose, the Cotati and Windsor basins under Santa Rosa, the Livermore basin, and the Great Valley. The pattern of shaking within the San Francisco Bay urban region also displayed a strong sensitivity to the hypocenter with significantly stronger shaking for north-to-south rupture compared to south-to-north rupture. Although we attribute some of this observation to the location of a majority of the urban area lying south of San Francisco and Oakland, the geologic structure also appears to play a significant role. Having characterized the ground motions generated by ruptures along the San Andreas fault on the west side of San Francisco Bay, in this study we focus on ground motions generated by ruptures of the Hayward, Rodgers Creek, and Calaveras faults on the east side of San Francisco Bay.

Larsen *et al*. (2000) simulated long-period ground motions for 20 Mw 7.0 scenario events on the Hayward fault using a simple 3-D seismic velocity model. They found high amplitude motions in the sedimentary basins, such as the San Pablo basin underneath San Pablo Bay, the Evergreen basin in the Santa Clara Valley, and the Livermore basin in the Livermore Valley. Harmsen *et al*. (2008) improved the characterization of ground motions from large earthquakes on the the Hayward fault by studying the long-period ($T > 1.0$ s) ground motions in the Santa Clara Valley from six scenario events that included variations in the magnitude, hypocenter, rupture speed, and seismic velocity model. These six scenarios were part of a large suite of 20 scenarios with ruptures on other faults in the region. The six Hayward earthquakes involved rupture of 57 km of the southern portion of the Hayward fault in Mw 6.9 and Mw 7.0

events. Harmsen *et al.* (2008) noted a strong dependence of the peak ground velocity on the hypocenter and significant basin amplification, particularly in the Evergreen basin east of San Jose.

Whereas Harmsen *et al.* (2008) focus on the variability of ground motions in the Santa Clara Valley for a variety of earthquake sources, including six Hayward fault ruptures, in this study we focus on the ground motions throughout the San Francisco Bay area for a larger suite of Hayward fault scenarios, some of which include rupture on additional faults. Harmsen *et al.* (2008) did not include the effects of large regions exhibiting aseismic creep on the coseismic slip distribution. As described in Aagaard *et al.* (XXXX) we include two different approaches that account for the effects of creep on the coseismic slip distribution. Thus, we build upon the efforts of Harmsen *et al.* (2008) in our suite of 37 scenarios by including variations in the rupture length, slip distribution, hypocenter, rise time, rupture speed, and how aseismic slip affects the coseismic slip distribution.

Wave Propagation Codes

Simulation of ground motions for the 37 scenario events involved five different ground-motion modeling groups, Aagaard, Graves, Larsen, Ma, and Rodgers and Petersson, each using a different wave propagation code. As we will discuss later, each group computed ground motions for two well-recorded moderate earthquakes and a common subset of the scenario earthquakes. These simulations demonstrate consistency among the modeling groups and permit tying together results from the different modeling groups' exploration of a subset of the scenarios. The codes employed by Aagaard, Graves, Larsen, and Rodgers and Petersson (Larsen and Schultz, 1995; Graves, 1996; Aagaard *et al.*, 2001; Nilsson *et al.*, 2007) were used in studies of the 1906 earthquake (Aagaard *et al.*, 2008a) and the 1989 Loma Prieta earthquake (Aagaard *et al.*, 2008b). Since the simulations of the 1906 earthquake, the code used by Rodgers and Petersson has been improved to include topography using a curvilinear grid approach (Appelö and Petersson, 2008). Ma previously applied his code (Ma and Liu, 2006) to study wave propagation in the 3-D heterogeneous structure of southern California (Ma *et al.*, 2008) and examine the effects of topography (Ma *et al.*, 2007).

Table 1 and Figure 1 summarize the modeling domains and features of the wave propagation codes used in this study. The domains generally span the region covered by the detailed portion of the USGS Bay Area Velocity Model 08.3.0, which we discuss in the next section. Graves and Larsen resolve waves with periods greater than 1.0 s, whereas Aagaard, Ma, and Rodgers and Petersson resolve periods greater than 2.0 s. Each of the modeling groups imposes a minimum shear-wave speed of 500 m/s to 700 m/s in their simulations. These choices for the minimum period and shear-wave speed reflect the computational resources available to each group and the overall efficiency of the wave propagation implementation.

The seismic velocity model includes topography, so the ground-motion simulations either explicitly include topography or warp the seismic velocity model by "squashing" the topography into a flat planar surface. In "squashing" the surface of the earth is deformed in the vertical direction so that the free-surface is flat and aligned at some elevation. This technique is preferable to the "bulldozing" approach which flattens the earth by stripping away all material above some elevation and filling in voids below this elevation with some generic material, because it retains near-surface low-velocity materials (Aagaard *et al*., 2008b).

As discussed in Part I, we use the cosine-sine slip-time function slip function developed by Liu *et al*. (2006),

$$D(t) = \begin{cases} D_f C_n \left(0.7t - 0.7\frac{\tau_1}{\pi}\sin\frac{\pi t}{\tau_1} - 1.2\frac{\tau_1}{\pi}\left(\cos\frac{\pi t}{2\tau_1} - 1\right)\right) & 0 \le t < \tau_1 \\ D_f C_n \left(1.0t - 0.7\frac{\tau_1}{\pi}\sin\frac{\pi t}{\tau_1} + 0.3\frac{\tau_2}{\pi}\sin\frac{\pi(t-\tau_1)}{\tau_2} + \frac{1.2}{\pi}\tau_1 - 0.3\tau_1\right) & \tau_1 \le t < 2\tau_1 \\ D_f C_n \left(0.3t + 0.3\frac{\tau_2}{\pi}\sin\frac{\pi(t-\tau_1)}{\tau_2} + \frac{1.2}{\pi}\tau_1 + 1.1\tau_1\right) & 2\tau_1 \le t < \tau \end{cases} \quad (1)$$

$$\dot{D}(t) = \begin{cases} D_f C_n \left(0.7 - 0.7\cos\frac{\pi t}{\tau_1} + 0.6\sin\frac{\pi t}{2\tau_1}\right) & 0 \le t < \tau_1 \\ D_f C_n \left(1.0 - 0.7\cos\frac{\pi t}{\tau_1} + 0.3\cos\frac{\pi(t-\tau_1)}{\tau_2}\right) & \tau_1 \le t < 2\tau_1 \\ D_f C_n \left(0.3 + 0.3\cos\frac{\pi(t-\tau_1)}{\tau_2}\right) & 2\tau_1 \le t < \tau \end{cases} \quad (2)$$

$$C_n = \frac{\pi}{1.4\pi\tau_1 + 1.2\tau_1 + 0.3\pi\tau_2} \quad (3)$$

$$\tau = 1.525 t_{95} \quad (4)$$

$$\tau_1 = 0.13\tau \quad (5)$$

$$\tau_2 = \tau - \tau_1 \quad (6)$$

where $D(t)$ is the slip at time t, D_f is the final slip, t_{95} is the rise time (as measured by the time it takes for 95% of the slip to occur), and τ, τ_1, τ_2, and C_n are constants.

Seismic Velocity Model

For this study we updated version 05.1.0 of the USGS Bay Area Velocity Model that we used for calculating the ground motions for the 1906 earthquake (Aagaard *et al*., 2008b; Aagaard *et al*., 2008a). Waveform modeling of moderate earthquakes (Mw 4-5) in the San Francisco Bay region showed that version 05.1.0 of the model predicted surface waves arriving about 5% faster than observed (Rodgers *et al*., 2008). Analysis of arrival times for small to moderate earthquakes and refraction shots confirmed a bias of about 5% too fast for both dilatational-wave speed (Vp) and the shear-wave speed (Vs) in version 05.1.0 of the model (Douglas Dreger, written comm., 2007). To quantify the discrepancy in wave speeds, we compared the wave speeds for each geologic unit in the seismic velocity model with the corresponding wave speeds from the Thurber *et al*. (2007) seismic tomographic model. We updated the relations between seismic wave speed and depth to improve the fit to the wave speeds and gradients in the Thurber

et al. (2007) tomography model at depths below several kilometers. We continued to use sonic well log data as the target at shallower depths where it provides tighter constraints.

Initial changes to the seismic velocity model did indeed reduce the travel times appropriately and essentially removed bias. However, several iterations were required to fine tune the velocities in the sedimentary units and to remove a spurious velocity contrast that had been introduced across the San Andreas fault in the La Honda Basin, which was inconsistent with 1989 Loma Prieta travel time observations. In the following paragraphs we summarize the major changes made to the velocity model to produce the updated 08.3.0 version used in this study. The electronic supplement contains the relations between wave speed and depth that update those in Brocher (2008).

1. For the upper mantle we decreased the wave speeds by 2.5% to better match the Thurber *et al*. (2007) tomographic model, and we added a small positive gradient based on seismic refraction results.

2. For the mafic lower crust/Great Valley ophiolite we reduced Vp in the upper 18 km by as much as 1 km/s and increased it below 18 km depth to a maximum of about 7.4 km/s.

3. For Franciscan units we reduced Vp at depths of 1–3 km by 1–2%, at depths of 4–10 km by 9%, and we increase Vp below 20 km by about 3%.

4. For granitic rocks above 2 km depth the velocities honor borehole sonic data, which is considered more reliable, whereas below 2 km we honored the gradient observed in the Thurber *et al*. (2007) tomographic model.

5. For Great Valley sequence units below 3 km the velocities honor the Thurber *et al*. (2007) tomographic model.

6. For Tertiary-Cenozoic sedimentary units at depths above 750 m we attempted to honor the Vp relation of Hartzell *et al*. (2006) for the Cupertino basin; otherwise, above 4 km depth the wave speeds honor the sonic well log data, which are considered more reliable than tomography at these depths; below 4 km the wave speeds honor the Thurber *et al*. (2007) tomography model.

7. For sedimentary units in the La Honda Basin, wave speeds were increased 10 to 20% except at depths greater than 6 km where it remains unchanged,

$$V_p = \begin{cases} 2.50 + 0.625d & \text{for } 0 < d \leq 4\text{km} \\ 5.00 + 0.200(d-4) & \text{for } 4\text{km} < d \leq 6\text{km} \\ 5.40 & \text{for } d > 6\text{km} \end{cases}, \tag{7}$$

where V_p is in km/s and d is depth in km. The sonic log for the Champlin Petroleum borehole indicates a Vp of 3.8 km/s at 1 km, a Vp of 4.2 km/s at 2 km, and a Vp of 4.7 at 3 km (Brocher *et al*., 1997). This borehole sampled a steeply dipping section of Butano sandstone for its entire length, so this sonic log may not be representative

of the basin as a whole. Williams *et al*. (1999) interpret a seismic refraction line along the La Honda Basin with the upper three 3 km of the basin modeled with a Vp of 4 km/s. The relations given by equation (7) yield slightly faster wave speeds than those for the Great Valley sequence units to a depth of 4 km. Between 4 and 6 km, the Vp lies between that for the Great Valley sequence units and the new Tertiary-Cenozoic sedimentary unit relation from the Cupertino Basin.

8. For Cenozoic sedimentary rocks near Half Moon Bay, we applied separate relations compared to other older Tertiary deposits in order to prevent very strong amplification that does not fit observations from the Loma Prieta earthquake.

9. We updated the attenuation quality factors, Qp and Qs, to the values given in Brocher (2008).

Testing with Moderate Earthquakes

In order to examine the ability of our long-period ground motion simulations to reproduce recorded velocity waveforms throughout the San Francisco Bay area we simulated two recent moderate earthquakes: the 31 October 2007 Mw 5.45 Alum Rock and 20 July 20 2007 Mw 4.18 Oakland events. These events occurred on the Hayward fault and were recorded throughout the area of interest for this study (Fig. 2). The Alum Rock event provides good sampling of the crust around the southern end of the Hayward Fault, while the Oakland event provides sampling of the crust around the northern end of the fault. The ruptures we consider in this study span the region between these events.

These moderate earthquakes are much smaller than our scenario events so that the event rupture processes are much simpler, which allows us to evaluate the seismic velocity model model and path propagation effects with relatively little bias due to source processes (e.g. spatial and temporal evolution of slip, rupture speed, and rise time). Furthermore, these events were recorded with a high signal-to-noise ratio and occur more frequently than large events. In general the simulations capture the main features of the observed ground motions and are consistent between modeling groups. Figure 2 shows the two earthquake locations and the stations for which we compare ground motion time histories.

The recorded motions for the Mw 5.45 Alum Rock earthquake show evidence of a finite-source process, so we construct a simple finite-source model for this event using the method of Dreger and Kaverina (2000). We compute Green's functions for the three-component displacement waveforms recorded at Berkeley Digital Seismic Network (BDSN) stations, BKS, CMB, PKD, and KCC with the GIL7 velocity model (Dreger and Romanowicz, 1994; Pasyanos *et al*., 1996). The Green's functions are convolved with a 0.3 second triangular slip velocity function. Both the observed waveforms and Green's functions are bandpass filtered between 0.01 to 0.3 Hz using a two-pole acausal

Butterworth filter. Assuming a rupture velocity of 2.8 km/s (approximately 0.80 Vs) yields a peak slip of 0.17 m, and a 7 km by 4 km (length by width) rupture patch. The slip extends downdip and to the southeast of the hypocenter (9 km depth), and was located between 9 to 13 km depth. The directivity associated with this rupture model derived from the waveform modeling is consistent with the directivity inferred from the spatial variation in peak horizontal ground accelerations and peak horizontal velocities (Seekins and Boatwright, 2007). This slip patch was projected onto the Hayward-Calaveras fault surface, which resulting in a close match between the strike and dip of the Berkeley focal mechanism and the strike and dip of the fault surface.

Each modeling group computed the waveforms at 185 stations for this event using the rupture model described earlier and the USGS Bay Area Velocity Model 08.3.0. Figure 3 illustrates the variation in shaking across the Santa Clara Valley that is accurately captured by the synthetic waveforms at stations CHR, Q32, H30, and CDOB for T $>$ 2.0 s. The electronic supplement includes plots of the synthetic and observed waveforms low-pass filtered with corner frequencies of 0.25 Hz (T $>$ 4.0 s) and 0.5 Hz (T $>$ 2.0 s) for all of the stations. For station CHR the observed horizontal velocities exceed the synthetic velocities by about 60%. Because this station sits only about 6.7 km from the epicenter, we attribute this discrepancy to our rupture model that simplifies the slip distribution and rupture propagation. For example, the rupture model may underestimate the amount of up-dip directivity.

The waveforms at station Q32, which sits in the Evergreen basin 10.8 km southwest of the epicenter, exhibit greater complexity than those at station CHR as a result of the complex basin response. The horizontal components are dominated by about 10 seconds of larger amplitude motion (peak velocities exceed 10 mm/s) followed by another 10 seconds of more moderate motion (peak velocities exceed 5 mm/s). The synthetic waveforms reproduce the variation in shaking but fail to capture details in the waveforms at periods near 2.0 s. The synthetics closely agree with the observed waveforms at periods of 4.0 s and greater (see the electronic supplement). Moving west across the Santa Clara Valley the seismic waves leave the Evergreen basin and near the western edge enter the Cupertino basin. At station H30, which sits 25.6 km southwest of the epicenter, Love waves (north-south component) dominate the ground motions with over 20 seconds of significant motion (peak velocities are near 5 mm/s). The synthetics reproduce the onset, amplitude, and duration of the motion; however, the later surface wave arrivals in the synthetics are slightly delayed relative to the observations. The synthetics at periods of 2.0 s and longer match the observations nearly as well as the synthetics at periods of 4.0 seconds and longer. In addition to the mismatch in later surface wave arrivals, the primary discrepancy is that the synthetics contain one additional cycle of relatively large amplitude motion associated with the surface waves compared to the observations.

The southward directivity results in lower ground motions north of the epicenter. As a result, the geologic structures tends to dominate the character of the shaking with less influence from the source. In this region the synthetics generally reproduce the amplitude and duration of motion at periods of 4.0 s and longer but struggle to reproduce the

waveforms at periods approaching 2.0 s. For example, at station CDOB in Livermore, 33.2 km north of the epicenter, reverberations within the Livermore sedimentary basin increases the duration of the shaking. The synthetics exhibit longer period motions than the observations even at periods of 4.0 s and longer, suggesting that the seismic velocity model does not adequately capture the geometry of the basin and/or variation of physical properties in and around the basin. Thus, the waveforms are not as accurate in this region as they are in the Santa Clara Valley.

In simulating the 20 July 2007 Mw 4.18 Oakland event we assess the ability of our simulations to reproduce the ground motions throughout the San Francisco Bay area to a source on the northern portion of the Hayward fault. For this event we employ empirical Green's function deconvolution of the records of a nearby Mw 2.7 event at two borehole stations, CMSB and SM2B. The observed moment-rate function at CMSB has much narrower pulse widths than SMCB, 0.14 s compared to 0.93 s. Based on the moment tensor of the event from the Berkeley Seismological Laboratory, the azimuth to CMSB and SM2B are 322 and 55 degrees, respectively; these stations sit nearly perfectly in the strike direction and the fault perpendicular directions. Assuming a rupture speed of 2.8 km/s we determine the rupture length from the fault perpendicular directivity relationship,

$$l = \tau_p 2.8 km/s = 2.6 km, \tag{8}$$

where τ_p is the pulse width. Similar to the Alum Rock event, the directivity inferred from waveform modeling is consistent with that inferred from the spatial variation in peak horizontal accelerations and peak horizontal velocities (Seekins and Boatwright, 2007). We choose a rupture width of 0.8 km based on a stress drop of 1.0 MPa, and the vertical strike-slip fault relationship between stress drop, scalar moment, and source dimension. These rupture dimensions yield a slip of 0.09 m with a rake of 168 degrees from the Berkeley Seismological Laboratory moment tensor solution. As in the case of the Alum Rock event, we project this slip patch onto the nonplanar geometry of the Hayward fault surface.

Figure 4 displays the observed and synthetic velocity waveforms at four sites (2190, BRK, BRIB, and CTA) for this event. The waveforms have been low-pass filtered with a corner frequency of 0.5 Hz (T $>$ 0.5 s). The electronic supplement contains plots of the observed and synthetic velocity waveforms for 115 stations low-pass filtered with corner frequencies of 0.5 Hz (T $>$ 2.0 s) and 0.25 Hz (T $>$ 4.0 s). Station BRK lies 9.7 km northwest of the epicenter less than a kilometer west of the Hayward fault and station CMSB (which we used to construct the source model). At this site the synthetics reproduce the simple velocity pulse present in the observed waveforms. Although this site displays the best match between the synthetics and observed waveforms, the synthetics at several other sites north of the epicenter also provide a good fit to the observed amplitude and duration of shaking, especially at periods of 4.0 s and longer.

Station 2190 sits 5.8 km south of the epicenter less than 2 km from the edge of San Francisco Bay. The synthetics capture the relative amplitude with the greatest motion associated with the shear-wave arrival but under-predict the amplitude and complexity, especially in the east-west component. For periods greater than 2.0 s, the observed peak velocity for the north-south component exceeds 1 mm/s whereas the peak velocity for the synthetics are all about 0.5 mm/s. At longer periods ($T > 4.0$ s) the discrepancy in amplitude between the observed and synthetic waveforms becomes smaller. We attribute this discrepancy to insufficient amplification in the simulations resulting from a combination of the minimum shear wave speed imposed in the simulations (which artificially stiffens the soft, near surface sediments) and complexity in the geologic structure not included in the seismic velocity model. For example, this region south of the epicenter between the San Francisco Bay and the Hayward fault may include locally softer or deeper alluvial sediments than regions north of the epicenter, where the synthetics closely follow the observed motions. The consistency among the modeling groups, however, remains excellent considering the variations in amplitude associated with different minimum shear wave speeds.

Shifting our focus to locations east of the Hayward fault, we find greater complexity in the observed waveforms, especially at shorter periods ($T > 2.0$ s). The simulations have difficulty reproducing this greater complexity; for example, at station BRIB (12.4 km northeast of the epicenter) the observed waveforms include a sharp initial arrival on the east-west component followed by an additional 15 s of shaking. The synthetics also include a sharp arrival on the east-west component but the arrival is more than a second later than the observed arrival. The synthetics display a similar overall duration of motion but do not replicate the details in the observed waveforms. Furthermore, we find slightly less consistency among the modeling groups but this is mainly limited to the vertical component. The greater complexity in the observed waveforms and delayed arrival of the shear wave in the synthetics suggests that the average shear wave speed east of the Hayward fault may be too slow in the seismic velocity model and the geologic structure may be significantly more complex than what is described by the seismic velocity model.

Further northeast at station CTA, 28.2 km from the epicenter, surface waves dominate the waveforms. The synthetics are able to replicate the amplitude and approximate duration of the surface waves but do a poor job of matching the details of the waveforms. In contrast to station BRIB, the arrival time of the shear wave in the synthetics for station CTA match the observed arrival time.

Accuracy of the Seismic Velocity Model

Examination of the waveforms across the region for the two events considered in this study suggests that the seismic velocity has the greatest accuracy in the Santa Clara Valley; in this region the synthetics match detailed features of the observed waveforms. Between the San Francisco Bay and the Hayward fault near Oakland, the simulations

fail to capture amplification at periods close to 2.0 s, indicating that the thickness of the unconsolidated Quaternary deposits in the seismic velocity model may need adjustment. Arthur Frankel (pers. communication) noted similar deficiencies between the San Francisco Bay and the Hayward fault slightly further south in 2-D simulations of the ground motions for the 6 September 2008 Mw 4.0 Alamo earthquake. Thus, ground motion simulations may underpredict the amplitude of the shaking in this region. East of the Hayward fault our simulations are only able to reproduce the amplitude and duration of the shaking; the seismic velocity model lacks sufficient detail to reproduce detailed features of the waveforms. The geologic structure east of the Hayward fault has yielded a more complex volume of Cenozoic and Mesozoic rocks compared to the volume dominated by Mesozoic rocks to the west of the fault (Graymer, 2000), so it is not surprising that the seismic velocity model needs to incorporate greater detail in this region. Hence, simulated ground motions from this region east of the Hayward fault are less accurate and provide an estimate of the amplitude and duration of shaking. This means they are less suitable for use as inputs in analyses where the details of the waveforms may be important.

In summary, these comparisons show that the USGS Bay Area Velocity Model version 08.3.0 reproduces important 3-D wave propagation features of the observed ground motions throughout the San Francisco Bay region at periods down to 2–4 seconds for two events along the Hayward fault. Rodgers *et al*. (2008) drew similar conclusions using version 05.1.0 of the model but noted a persistent bias in the wavespeeds as discussed earlier. Kim *et al*. (XXXX) demonstrated that version 08.3.0 reduces the average bias in arrival times compared with version 05.1.0 while maintaining a good fit to the peak horizontal velocities over five orders of magnitude for moderate earthquakes. Furthermore, the consistency in ground motions among the five modeling groups using different numerical methods and implementations implies that we can use the results from any of the modeling groups to characterize the ground shaking in our large scenario events.

Scenario Earthquakes

Table 2 summarizes the 37 events in our suite of earthquake scenarios. Aagaard *et al*. (XXXX) discuss each of the earthquake source parameters and the rationale for the choice of variation in detail. In this section we discuss the general trends in the ground motions and the sensitivity in the shaking to variation of the earthquake source parameters for the long-period ($T > 1$–2 s) simulations. The following section discusses the broadband ($T > 0.1$ s) simulations in the context of the 1868 earthquake and the Next Generation Attenuation (NGA) ground-motion prediction equations.

Base Cases

With the modeling groups examining a different subset of the suite of scenario earthquakes, we first demonstrate the consistency of the shaking intensity and velocity waveforms among the modeling groups for one of the scenarios. This extends the consistency we found for the Mw 5.4 Alum Rock and Mw 4.2 Oakland earthquakes to our larger scenarios that have more complex rupture models. Figure 6 shows maps of the Modified Mercalli Intensity (MMI) for scenario HS G01 HypoH from the Graves, Larsen, Ma, and Rodgers modeling groups and residuals with respect to Aagaard's MMI values; a map of MMI for Aagaard's simulation is shown in Figure 8. For consistency with the other modeling groups we use only the long-period ($T > 1.0$ s), deterministic portion of Graves's broadband simulation.

The amplitude and spatial variation of the shaking intensities are very similar among the groups with mean residuals less than 0.20 MMI units. The standard deviations in the residuals for Graves's and Larsen's simulations are about 0.50 MMI units because both of these simulations include periods down to 1.0 s, whereas Aagaard's simulations include periods down to only 2.0 s. The standard deviations in the residuals for Ma's and Rodgers's simulations are smaller with values of about 0.30 MMI units, because they use the same minimum period of 2.0 s as Aagaard's simulations. The largest discrepancies among the modeling groups arises in the Great Valley east of the San Francisco Bay. The longer propagation distances for this region coupled with greater attenuation results in lower amplitudes of shaking for the Larsen and Graves modeling groups which include intrinsic attenuation. Similar levels of agreement are obtained for the other scenarios, and the electronic supplement contains plots comparing the shaking intensities among the modeling groups for bilateral rupture of the Hayward South + North rupture length.

Velocity waveforms at sites throughout the San Francisco Bay area (plots for three sites are shown in Figure 7 with plots for 80 sites available in the electronic supplement) illustrate that, in addition to agreeing in amplitude, the modeling groups generate waveforms with the same features. The first arrivals are nearly identical. We find good agreement in the amplitude and duration of most later arrivals, but inclusion/exclusion of attenuation and topography and different minimum shear wave speeds leads to small discrepancies in the arrival times for the surface waves. Larsen's waveforms include large secondary arrivals at some locations, which appears to be related to simulating ruptures with significant energy at 1.0 s while including topography.

The close agreement in the amplitude, duration, and features of the waveforms across the modeling groups means that we can use scenarios HS G01 HypoH and HS+HN G04 HypoO to tie the results of the different modeling groups together. We use different groups to characterize the sensitivity of the ground motions to different source parameters, with Aagaard's simulations for rupture length and slip distribution, Graves's simulations for rupture length and hypocenter at broadband frequencies, Larsen's simulations for rise time, and Ma's simulations for rupture speed. While the results of each modeling group can be used to independently examine the sensitivity of the ground motions

to a single parameter or a small subset of the parameters, we rely on the consistency among the modeling groups to establish the relative sensitivity of the ground motions to variation of the rupture length, slip distribution, hypocenter, rise time, and rupture speed.

Rupture Length, Slip Distribution, and Hypocenter

Aagaard's simulations include 25 earthquake scenarios that provide a comprehensive view of the ground motions for the five different rupture lengths with one to three hypocenters per rupture length and two to three slip distributions per hypocenter. The rupture length (which correlates with magnitude) exerts the greatest influence on the amplitude of shaking, with longer rupture lengths (larger magnitude earthquakes) generating stronger shaking as evident in Figures 8 and 11. Scenario HS G01 HypoH causes shaking greater than or equal to MMI VII over about 24% of the San Francisco Bay urban area. MMI VII corresponds to the approximate shaking intensity when modern structures begin to suffer damage. The fraction of the urban area experiencing MMI VII increases to 33% in scenario CC+HS G03 HypoH, 58% in scenario HS+HN G04 HypoO, and 60% in scenario HS+HN+RC G06 HypoSPB. We attribute these high levels of shaking experienced by such large fractions of the urban area to the Hayward fault running directly through the urban corridor along the eastern edge of the San Francisco Bay.

The slip distribution has less influence on the overall distribution of shaking, but changes in location of large slip patches affect the shaking close to the rupture. The features in the maps of MMI in Figure 8 closely resemble each other for corresponding rupture lengths and hypocenters with different slip distributions (one uses a background slip distribution with a vertical gradient in slip to account for creep paired with one stochastic distribution and the other uses a background slip distribution with the slip-predictable approach for accounting for creep paired with another stochastic distribution). These same observations hold for the other hypocenters for the Hayward South, Hayward South + North, and Central Calaveras + Hayward South rupture lengths and changing the random seed in the stochastic slip distribution with the same vertical gradient in slip for the Hayward South rupture length (see the electronic supplement).

For the Hayward South, Hayward South + North, and Central Calaveras + Hayward South rupture lengths, we consider three hypocenter locations. This yields cases with north-to-south rupture, bilateral rupture, and south-to-north rupture. As shown in Figure 10 rupture directivity along the strike of the fault causes the ground motions to be much smaller in the San Jose area for south-to-north rupture compared with north-to-south or bilateral rupture. Likewise, the ground motions around San Pablo Bay are much smaller for north-to-south rupture compared with bilateral or south-to-north rupture. These trends are consistent with previous studies of rupture directivity (Somerville *et al*., 1997; Aagaard *et al*., 2001; Spudich and Chiou, 2008). In our discussion of Graves's broadband ground motions in a

later section, we will examine the spatial variation in spectral acceleration for the different hypocenters in the context of the Spudich and Chiou (2008) directivity corrections to the NGA ground-motion prediction equations.

Graves's broadband velocity waveforms illustrate these trends in rupture directivity. In San Francisco the ground motions are largest for south-to-north rupture (Fremont epicenter) for both the Hayward South and Hayward South + North rupture lengths, consistent with larger ground motions for ruptures propagating towards the city. The waveforms in Livermore tend to be largest for north-to-south rupture, because Livermore lies north of the more rigid rock underneath the hills east of San Jose. This more rigid material tends to trap energy in the Livermore basin in north-to-south ruptures and shield Livermore from energy radiated in south-to-north ruptures. The waveforms in Livermore are also sensitive to the slip distribution. For the Hayward South + North rupture length and Fremont epicenter, the velocities are less than about 0.2 m/s with a duration of only about 15 s, whereas the amplitudes reach 0.8 m/s with 50 s of significant shaking for the San Pablo Bay epicenter; yet, the ground motion amplitudes and duration of shaking for the three epicenters and the Hayward South rupture length are quite consistent, with amplitudes of about 0.15 m/s. We attribute these different sensitivities to the hypocenter to the different stochastic portions of the slip distribution in the two sets of scenarios. For the Hayward South + North rupture length, there are no large slip patches south of Livermore, so rupture starting in Fremont does not radiate significant energy until it is further north. In the case of the Fremont epicenter for the Hayward South rupture length, there is a large slip patch at the southern end of the rupture, so northward propagating ruptures radiate energy into the Livermore area.

Some features in the distributions of shaking persist as we vary the rupture length, slip distribution, and hypocenter. These features are related to geologic structure as opposed to source features. This includes higher intensity shaking extending 20–40 km east of the Hayward fault due to deeper soft material east of the fault compared to west of the fault. We also find higher intensity shaking in the sedimentary basins, such as the Livermore basin, the San Pablo basin under San Pablo Bay, the Evergreen basin east of San Jose, and the Cupertino basin west of San Jose. The shaking intensities in the Evergreen and Cupertino basins reach values 1–2 MMI units higher than locations several kilometers outside the basins. Similarly, the river valleys north of San Francisco Bay (e.g., Napa River valley running northwest from Napa) tend to have intensities 1–2 MMI units higher than the surrounding areas.

Larsen *et al.* (2000) also found amplification of ground motions in the San Pablo, Evergreen, and Livermore basins for magnitude 7.0 Hayward fault scenario earthquakes using a very simple 3-D seismic velocity model. Using seismic velocity models defined nearly identical to the USGS Bay Area Velocity Model 08.3.0, Harmsen *et al.* (2008) observed persistent patterns of shaking very similar to those in this study for scenario earthquakes involving the Hayward and Calaveras faults. The ruptures excite surface waves that are amplified in the Livermore, Evergreen, and Cupertino basins. Furthermore, Harmsen *et al.* found high intensities extending south along the east side of the Santa Clara Valley from the Evergreen basin as we do in this study.

Rise Time and Rupture Speed

Larsen's simulation of eight scenarios with four different rise times for Hayward South and Hayward South + North bilateral ruptures characterize the sensitivity of the ground motions to the rise time in the slip time history (duration of slip at a point). For each rupture length, we consider three different scaling factors of 1.0, 1.5, and 2.0 in the expression for the rise time as a function of slip,

$$\frac{t_{95}}{t_0} = C\sqrt{\frac{D_f}{D_0}}, \tag{9}$$

where t_{95} denotes the time for 95% of the slip to occur, D_f denotes the final slip, t_0 = 1.0 s, D_0 = 1.0 m, and C takes on values of 1.0, 1.5, or 2.0 (denoted by Tr10, Tr15, and Tr20 in the scenario labels). This provides a factor of two difference in rise times across the scenarios with the median rise time in each scenario similar to the value proposed by Somerville *et al*. (1999) for self-similar rupture. We also consider uniform rise times, $t_{95} = 1.0s$ for the Hayward South rupture length (denoted by Tr10u in the scenario name) and $t_{95} = 2.0s$ for the Hayward South + North rupture length (denoted by Tr20u in the scenario name).

The ground motions exhibit very little sensitivity to the rise time. Figure 12 shows that the velocity amplitudes can vary up to about 50% for variation in rise times by a factor of two. Varying the rise time without any corresponding changes in any of the other source parameters does not change the shape of the waveforms. These variations are much less dramatic than the changes we observed for the variations in rupture length and hypocenter. The electronic supplement contains waveforms at 80 sites and maps of the shaking intensity which demonstrate that all of the sites display similarly weak sensitivities to the rise time. Aagaard *et al*. (2001) arrived at the same conclusion through variation of the peak slip rate in simpler rupture models in a model with 1-D structure.

We characterize the sensitivity of the ground motions to the rupture speed using Ma's six simulations with three rupture speeds for Hayward South and Hayward South + North bilateral earthquake ruptures. The scenarios include local rupture speeds in high slip regions at 82% of the local shear wave speed (denoted by Vr82 in the scenario name), 92% of the local shear wave speed (denoted by Vr92 in the scenario name), and supershear rupture (denoted by Vr141 in the scenario name). Part I (Aagaard *et al*., XXXX) discusses the details of the local rupture speed variation. The two subshear cases (Vr82 and Vr92) span the range of typical rupture speeds for crustal strike slip events. The supershear case includes locally supershear rupture where the slip exceeds the average slip with a maximum rupture speed of $\sqrt{2}$ times the local shear-wave speed at the location with the maximum slip.

The amplitude of the velocity waveforms display roughly the same sensitivity to the variations in rupture speed as they do to variations in rise time. However, ruptures with faster rupture speeds radiate energy in a shorter time period, which results in sharper arrivals and shorter duration velocity pulses. This gives rise to some small changes in the shape of the waveforms as evident in Figure 13 for bilateral Hayward South + North ruptures. The waveforms in

San Francisco and Livermore, which lie well off the strike of the Hayward fault display less variation in shape than those in San Jose, which lies close to the southern end of the rupture and is more sensitive to the rupture duration. At sites very close to the rupture, we do not find evidence for rotation of the peak motion from fault-perpendicular (see velocity waveforms in the electronic supplement) as predicted in theoretical models of supershear rupture (Dunham and Archuleta, 2004; Aagaard and Heaton, 2004). This is likely due to the relatively short bursts of supershear in our rupture models and complexity of the velocity waveforms associated with the 3-D geologic structure.

Creep and Coseismic Slip

Most of the earthquake scenarios use the vertical gradient in slip in creeping regions to account for how creep may affect the coseismic slip distribution. As discussed in Part I (Aagaard *et al*., XXXX), the vertical gradient decreases the slip in creeping regions as the rupture propagates into shallower regions. We chose the vertical gradient of -0.12 m/km for consistency with the paleoseismic record and the reduced area factor developed by the WGCEP (2003). Although we expect creep, which accommodates some of the long-term fault slip-rate, to exert some influence on the coseismic slip distribution, its effect could be minimal. At the other end of the spectrum, perhaps very little or no coseismic slip occurs in the creeping regions. Neglecting the influence of creep corresponds to a vertical gradient in slip of zero, whereas preventing coseismic slip in creeping regions corresponds to an infinite vertical gradient in slip. As the vertical gradient in slip increases, slip in the creeping regions decreases, which reduces the average slip and earthquake magnitude. We consider both of these end-member cases for bilateral rupture of the Hayward South and Hayward South + North rupture lengths.

For the Hayward South + North rupture length, the moment magnitude of the scenario without coseismic slip in creeping regions (fully creeping) is 6.82, the moment magnitude of the scenario with a gradient of -0.12 m/km is 7.05, and the moment magnitude of the scenario neglecting creep is 7.12. Figure 14 displays maps of the MMI for these three scenarios and Figure 15 shows the velocity waveforms at three sites. The shaking intensity and velocity amplitudes follow the variation in magnitude. The values for the Mw 6.82 scenario are similar to those for the bilateral Mw 6.76 Hayward South scenario, and the values for the Mw 7.12 scenario are slightly higher than those for the Mw 7.05 scenario. Because we use the same random seed in the stochastic portion of the slip distribution, the differences are limited to the amount of slip and the relative distribution between the creeping and locked portions. In the fully-creeping scenario, very little slip occurs near the surface. Consequently, the rupture generates smaller amplitude surface waves, so the velocities in Livermore are about one-third to one-half of those in the scenarios in which creep exhibits less influence on coseismic slip. Similarly, the velocities are about 50% smaller in San Jose for fully-creeping scenario. The corresponding ground motions for the Hayward South rupture length display similar trends.

The simulations suggest that the ground motions are only moderately sensitive to the presence of the creeping regions if creep has a moderate to minimal impact on the coseismic slip distribution. This would likely be the case in regions with only very shallow creep or regions where the creep rate is a small fraction of the long-term fault slip rate. On the other hand, if creeping regions prevent coseismic slip with rise times comparable to locked regions, the expected magnitudes of Hayward fault events are about 0.1-0.2 units smaller with a corresponding decrease in the intensity of the shaking with even smaller excitation of surface waves.

Broadband Simulations

Graves extended his simulations of the six Hayward South and Hayward South + North scenarios to shorter periods using the hybrid procedure described in Graves and Pitarka (2004). This simulation technique combines a stochastic approach at short periods (0.1 s $<$ T $<$ 1 s) with the 3-D deterministic approach described earlier at long periods (T $>$ 1 s) to produce broadband ground-motion synthetics. We also employed this methodology to calibrate the wavenumber at which we cross-over from the nominal, background slip distribution to the stochastic slip distribution in Part I (Aagaard *et al*., XXXX).

In the short-period simulations we sum the response for each subfault assuming a random phase, an omega-squared source spectrum, and simplified Green's functions calculated for a specified 1-D velocity structure. This approach follows from Boore (1983) with the extension to finite faults given by Frankel (1995) and Hartzell *et al*. (1999). Each subfault ruptures with a moment proportional to the final slip of the subfault given by the original source model, and the values are scaled uniformly so that the moment matches that of the original source model.

As discussed in the previous section, the creeping portion of the fault requires special attention when developing the kinematic rupture model. Furthermore, the simulation of high frequency motions using the semi-stochastic approach of Graves and Pitarka (2004) also must account for this effect. In determining the effective area and magnitude of the rupture, we use the area reduction factor (R) used by the WGCEP (2003). In the semi-stochastic simulation, the moment release of each subfault scales with the high frequency stress parameter, σ_p ((Boore, 1983). Following self-similarity the moment also scales as Area$^{3/2}$, or R$^{3/2}$. Thus, in order to properly account for the creeping portions of these ruptures, the stress parameter must also be scaled by R$^{3/2}$. Our default value for the stress parameter is 50 bars. For the Hayward South ruptures, R=0.79, which yields a stress parameter for these ruptures of 35 bars; for the Hayward South+North ruptures, R=0.86, which yields a stress parameter for these ruptures of 40 bars.

The formulation requires the specification of a 1-D layered velocity model in calculating simplified Green's functions and impedance effects. In this study we create a 1-D velocity model that roughly follows the average depth variations in the 3-D structure, and we include both direct and Moho-reflected rays, which are attenuated by 1/Rp,

where Rp is the total path length traveled by the particular ray. For each ray we compute a radiation pattern coefficient by averaging over a range of slip mechanisms and takeoff angles. Anelasticity is incorporated via a travel-time weighted average of the Q values for each of the material layers and a generic rock site spectral decay operator, κ=0.04 (Anderson and Hough, 1984). Finally, gross impedance effects are included using quarter wavelength theory (Boore and Joyner, 1997) to derive amplification functions that are consistent with the specified 1-D velocity structure.

To account for site-specific geology in the broadband motions, we apply frequency-dependent, non-linear amplification factors based on Vs30, the travel-time-weighted shear speed in the upper 30 m at the site. The site-specific Vs30 values were taken from the map of Wills *et al*. (2000). The form of the amplification factors were developed using equivalent linear site response analysis (Walling *et al*., 2008) as implemented in the NGA ground-motion prediction equations of Campbell and Bozorgnia (2008).

Comparison with the 1868 Earthquake

Although we are not attempting to simulate the 1868 Hayward fault earthquake in detail (because little is known about its source parameters), several of the scenarios are designed to have source parameters that might be similar to this event. The Hayward South scenarios are consistent with the rupture length (Yu and Segall, 1996; Bakun, 1999) and magnitude (Bakun, 1999) of the 1868 earthquake. Boatwright and Bundock (2008) suggest that the north-south symmetry of the intensities is consistent with bilateral rupture compared with either predominantly north-to-south or south-to-north rupture. Our selection of three hypocenters permits further analysis to identify which rupture propagation pattern is most consistent with the shaking intensities from the 1868 event.

Figure 16 compares Modified Mercalli Intensity from Graves's broadband ($T > 0.1$ s) simulations of three Mw 6.76 Hayward South ruptures (HS G01 HypoO, HS G01 HypoH, and HS G01 HypoF) with the intensities of the 1868 earthquake compiled by Boatwright and Bundock (2008). The limited number of intensity observations (125) and unknown slip distribution for the 1868 earthquake limit the level of agreement, but the simulation with bilateral rupture (Hayward epicenter) produces intensities most consistent with those from the 1868 earthquake. However, all three Mw 6.76 scenarios fit the 1868 intensities relative to the uncertainty in the slip distribution and our expectations based on our previous efforts to match MMI values for the Loma Prieta earthquake (Aagaard *et al*., 2008b). Comparison with Mw 7.05 scenario earthquakes with the Hayward South + North rupture length (shown in the electronic supplement) exhibit significantly less consistency with the observed intensities from the 1868 earthquake. Thus, the simulations support previous studies (Bakun, 1999) that assign a magnitude of about 6.8 to the 1868 earthquake.

Comparison with NGA Models

Comparison of the broadband ground motions with ground-motion prediction equations, such as the NGA relations (Abrahamson and Silva, 2008; Boore and Aktinson, 2008; Campbell and Bozorgnia, 2008; Chiou and Youngs, 2008), provides an additional perspective from which to assess the ground motions for our scenario events. We will use AS08, BA08, CB08, CY08 to refer to these four NGA relations, respectively. In calibrating the earthquake source parameters via comparison of broadband synthetics from a 1-D velocity model with the NGA relations, we focused on minimizing the mean residual, not the variance or spatial variation. The broadband synthetics for the six scenarios that incorporate variability in the hypocenter (rupture directivity) and magnitude, permit a much more detailed comparison, including examination of effects due to basin response, local site conditions, and rupture directivity.

Figure 17 compares spectral accelerations (SA) at a period of 1.0 s from Graves's broadband simulation of the Mw 6.76 Hayward South bilateral rupture (scenario HS G01 HypoH) with those predicted by the AS08, BA08 and CB08 NGA relations. The mean residuals correspond to event terms in the ground-motion prediction models and express how the average ground motions from the 3-D simulations differ from the median of the ground motion prediction model for the specified earthquake magnitude.

The mean residual for each of the three NGA relations is small with the peak in the histogram within about 0.2 $\log_2$ units (15%) of zero. The maps of the residuals clearly show that the 3-D ground motion simulations predict stronger shaking off the ends of the rupture than the NGA ground-motion prediction equations. The 3-D ground motion simulations include strong along-strike directivity which is not explicitly included in the NGA relations. The NGA relations incorporate the distance from the rupture, so that the spectral values average the directivity effects along the fault strike. In the next section we examine this issue in more detail using Graves's broadband simulation of three the Hayward South + North ruptures.

We examine the variation in the residuals of the spectral acceleration with period for the BA08 NGA relation using the Graves's Hayward South + North ruptures (Figure 18. The electronic supplement contains similar plots for peak horizontal ground acceleration (PGA), peak horizontal ground velocity (PGV), and spectral acceleration at periods of 0.3 s, 1.0 s, and 3.0 s for each of Graves's broadband simulations and the AS08, BA08, and CB08 NGA ground-motion prediction equations. At shorter periods (0.3 s) the variance is quite small (0.44 $\log_2$ units or 36%), and it increases considerably with increasing period (0.71 $\log_2$ units or 64% at a period of 1.0 s and 1.06 $\log_2$ units or 110% at a period of 3.0 s). A similar trend was seen in the analysis of the Mw 7.8 San Andreas ShakeOut simulations for Southern California (Graves *et al*., 2008). In that study, as in the current study, the large variances at the longer periods are primarily due to the effects of rupture directivity and amplification within relatively low shear wave velocity material, such as sedimentary basins. These are robust features of the 3-D long-period deterministic ground-motion simulations

that we associate with the 3-D geologic structure and source characteristics. The NGA models incorporate such effects via very simple approximations as we discuss in the following two sections.

We summarize the consistency of the simulations with the three NGA relations in Figure 19 by computing the mean residual and its variance averaged over the three NGA relations for Graves's six broadband simulations (scenarios HS G01 HypoO, HS G01 HypoH, HS G01 HypoF, HS+HN G04 HypoSPB, HS+HN G04 HypoO, and HS+HN G04 HypoF). In general, the simulated motions fall about one standard deviation above the median value, suggesting that, on average, the simulations are within the expected range of event-to-event variability observed in recorded earthquakes of the same magnitude. The synthetics likely exceed the median NGA values due to the relatively narrow rupture width for the Hayward fault (we linear taper the slip from 1 to 0 from 13 km to 16 km depth). The smallest mean residuals generally occur for the southernmost epicenter (Fremont) for both the Mw 6.76 and Mw 7.05 scenarios. We suspect this results from trade-offs between the assumed hypocenters, the kinematic slip distribution, and the interaction of the seismic waves with the 3-D geologic structure. We hesitate to draw any broad conclusions about the variations in the mean residuals without applying the broadband simulation methodology to the entire suite of scenarios that incorporate greater variability in the rupture parameters. Furthermore, it is difficult to assess how one might adjust the NGA models to account for the effects of creep on coseismic slip.

Accounting for Directivity

As discussed earlier, at the longer periods the simulated motions generally exceed the empirical ground-motion relations in regions with strong forward directivity and fall slightly below the empirical relations in regions with backward directivity; consequently, the PGV and spectral acceleration at 1.0 s and 3.0 s at most sites are highly sensitive to the hypocenter. Figure 18 clearly illustrates this effect by comparing the Mw 7.05 bilateral Hayward South + North rupture with the BA08 NGA relation for spectral acceleration at 1.0 s. While the overall mean of the residuals for these cases is in the range of 10% to 20%, sites located in the forward rupture direction have simulated motions up to 2–3 times larger than the empirical relation, whereas sites in the backward rupture direction can have motions 2–3 times smaller than the empirical relation.

Somerville *et al.* (1997) was the first to develop a directivity model that could be applied as a correction to ground-motion prediction equations. Two additional directivity models have been developed in conjunction with the NGA program, Spudich and Chiou (2008) proposed a model based on isochrone theory and Rowshandel (XXXX) proposed a model based on rupture heterogeneity and source-site geometry. The Spudich and Chiou and Rowshandel corrections give similar results, although the Rowshandel model generally predicts stronger directivity effects, particularly for ruptures containing strong slip asperities.

Figure 20 shows the Spudich and Chiou directivity corrections for the three Mw 7.05 Hayward South + North scenarios applied to the BA08 NGA relation for 1.0 s SA. The pattern of these corrections corresponds quite well to the residuals shown in Figure 20, but the absolute level is smaller with the maximum correction not exceeding about 25%. Consequently, applying these corrections to the NGA relation only reduces the standard deviation of the residuals by a few percent. Similar results are found for PGV and 3.0 s SA, as well as for the other NGA relations (see the electronic supplement).

We attribute the differences in the strength of the rupture directivity to several factors, all of which arise from the fact that there are relatively few ground-motion recordings close to large strike-slip earthquake ruptures. We developed our rupture models using information gleaned from source inversions of past earthquakes as well as theoretical and laboratory analyses of rupture dynamics (see Aagaard *et al.* (XXXX)). We calibrated the models to match, on average, existing ground-motion records. However, the sparsity of data can leave some details of the rupture process rather poorly constrained. For example, it is generally accepted that ruptures tend to propagate at a speed of about 80% to 85% of the local shear-wave speed; however, it is not uncommon for ruptures to propagate slower than this and there are several cases where supershear rupture has been proposed (Olson and Apsel, 1982; Archuleta, 1984; Spudich and Cranswick, 1984; Anderson, 2000; Bouchon *et al*., 2000; Bouchon *et al*., 2001; Sekiguchi and Iwata, 2002; Bouchon and Vallee, 2003; Dunham and Archuleta, 2004; Ellsworth *et al*., 2004; Aagaard and Heaton, 2004). Unfortunately, the existing catalog of ground-motion records fails to provide comprehensive constraints on the nature of this variability.

This lack of data also led Spudich and Chiou to make simplifying assumptions in the development of their directivity model, such as truncating the data (and model) at a distance of 40 km from the rupture. This precluded any period dependence in the directivity pattern; we expect longer period ground motions, e.g., surface waves, to display directivity effects at much greater distances from the source than shorter period ground motions. Additionally, they also assumed a fixed value for the rupture speed of 0.80 Vs. Aagaard and Heaton (2004) demonstrated that rupture directivity effects become stronger as the rupture speed approaches the local shear wave speed. Since our kinematic Hayward ruptures generally propagate in the range of 80% to 90% of the local shear-wave speed, compared to the 80% value used for the Spudich and Chiou corrections, this may explain some of the difference seen in the residuals. Spudich and Chiou also found considerable variability in the amount of directivity in the observed data. For example, records from the 1979 Mw 6.5 Imperial Valley and 1989 Mw 6.9 Loma Prieta earthquakes exhibit a strong positive correlation with the isochrone directivity parameter, but the records from the 1995 Mw 6.9 Kobe earthquake exhibit a weak negative correlation. This suggests that the simulations may not over-predict the rupture directivity, but rather a more comprehensive directivity model may need to consider amplification variations as a function of rupture speed and distance.

Basin Response

Within sedimentary basins the simulated PGV and spectral accelerations at 1.0 and 3.0 s consistently exceed the empirical predictions by a factor of up to 2 to 3. This is also true in some regions outside sedimentary basins, such as the area just east of the Hayward fault between Livermore and Concord (see Figure 18 and the electronic supplement), which is composed of material with low shear-wave speeds compared to the surrounding rock. The NGA models account for basin amplification either through Vs30 alone (BA08) or through a combination of Vs30 and a basin depth term (AS08, CB08, CY08). However, most of the ground-motion data used to constrain these models come from deep basins (e.g., the Los Angeles basin) or theoretical studies within deep basin environments (Day *et al.*, 2008). In addition, the models also do not explicitly account for basin-edge effects or the coupling of directivity and basin amplification.

In the development of their ground-motion model, Boore and Aktinson noted the strong correlation between Vs30 and basin depth in the NGA data set and argued that Vs30 can be used as a proxy for basin depth in the empirical regression. While this is true for the NGA data set in general, it may not hold for the greater San Francisco Bay area where the basins are relatively shallow compared to other regions (Figure 21). In this context basin depth is defined as the depth to the 1.5 km/s shear-wave isosurface, hereafter referred to as Z1.5. For the San Francisco Bay area we measured Z1.5 in the 3-D USGS Bay Area Velocity Model 08.3.0 on a grid of sites at 1 km spacing and estimated Vs30 for each site using Wills *et al.* (2000). Because Wills *et al.* classify sites into discrete Vs30 bins, we totaled the number of observations within each bin and scaled the symbols in Figure 21 by that number. While the NGA data set shows a clear and strong increase of Z1.5 with decreasing vs30, the Bay area sites exhibit a very weak correlation. This could reflect errors in the construction of the seismic velocity model or differences in the tectonic environments between the San Francisco Bay area and the sites in the NGA data set.

We explore the implications of this difference in correlation to determine how well it explains larger amplitude ground motions in the 3-D simulations compared with the NGA ground-motion prediction equations. We derive an approximate amplification correction to the Boore and Aktinson NGA model for our San Francisco Bay sites. First, we find the correlation between Vs30 and Z1.5 noted by Boore and Aktinson using the following relational form:

$$\log_{10}(Vs30/V_0) = A + B\log_{10}(Z1.5/Z_0), \tag{10}$$

where V_0 = 760 m/s, Z_0 = 1 km, A = -0.375, and B = -0.211. Given the Z1.5 data for the San Francisco Bay area, we use this relation to compute Vs30 at our sites that would be consistent with the NGA data set. In other words, we replace the Vs30 values from Wills *et al.* with Vs30 values ($Vs30_{pred}$) predicted by Z1.5 and the correlation between Vs30 and Z1.5 in the NGA data set. For linear site response the BA08 amplification term is given by

$$A_{site} = \left(\frac{Vs30_{site}}{V_0}\right)^x \tag{11}$$

where $Vs30_{site}$ would be the site-specific Vs30 value (from Wills *et al.*, for example). For periods longer than about 1 second x is approximately constant and equal to -0.725. From this relation we define an approximate amplification correction to the BA08 NGA relation for our sites as

$$A_{cor} = \frac{A_{pred}}{A_{site}} = \left(\frac{Vs30_{pred}}{Vs30_{site}} \right)^{x}. \quad (12)$$

Figure 21 shows the spatial distribution of A_{cor} for our model region. Comparing this to the residuals for spectral acceleration at 3.0 s for the Mw 7.05 Hayward South + North scenario shown in Figure 18, we see many similarities both in terms of spatial pattern and amplitude (keeping in mind that the residuals in the figures also contain the effects of rupture directivity). The residuals indicate amplification of motions along the eastern side of the Hayward fault, which extends north into the San Pablo Basin and south toward Gilroy. The region immediately east of the Hayward fault has relatively high Vs30, but also relatively deep Z1.5; thus, the NGA relations (without the amplification correction) tend to under-predict the simulated motions in this region. Likewise, regions surrounding the margins of the San Francisco Bay and the Sacramento River Delta have relatively low Vs30 but a relatively shallow Z1.5. This leads the NGA relations over-predicting the simulated motions in these regions. Other regions where Vs30 and Z1.5 tend to be correlated, such as the Cupertino and Evergreen basins near San Jose and the Great Valley, the NGA relations are similar to the simulated motions. This suggests that refinement of the ground-motion prediction models may be required in order to adequately account for the effects of amplification across the diverse range of tectonic environments, including shallow basins.

Conclusions

The ground-motion simulations demonstrate that larger Hayward fault earthquakes generate strong shaking throughout the San Francisco Bay area with about 50% of the urban area experiencing MMI VII or larger for magnitude 7.0 earthquakes. The details of the shaking are strongly dependent on the rupture length (or earthquake magnitude), hypocenter (or rupture directivity), and slip distribution. The ground motions exhibit a relatively weak sensitivity to variations in the rise time, consistent with results from a previous study using a generic 1-D variation in material properties (Aagaard *et al.*, 2001). The ground motions also display a relatively weak sensitivity to the rupture speed; we do not find evidence for regions in the San Francisco Bay area with a strong sensitivity to the rupture speed, such as that found in the Los Angeles basin for northwest rupture of the southern San Andreas fault (Graves *et al.*, 2008).

The simulations predict ground motions consistent with the Abrahamson and Silva (2008), Boore and Aktinson (2008), and Campbell and Bozorgnia (2008) NGA ground-motion prediction equations with two areas of departure. The 3-D simulations generate stronger rupture directivity than that predicted by the Spudich and Chiou (2008) directivity correction to the NGA relations, although the spatial variation in ground motion in the simulations associated with

rupture directivity closely matches the spatial variation in the Spudich and Chiou model. Similar discrepancies exist with respect to individual events used to construct the Spudich and Chiou model, suggesting that the accuracy of the model could be improved by incorporating a period dependence on the areal extent of directivity effects and a rupture speed other than 80% of the shear-wave speed. Analysis of ground-motion amplification in sedimentary basins from our simulations indicates that amplification in shallow basins (e.g., the Cupertino and Evergreen basins near San Jose, the San Pablo and San Leandro basins near Oakland, and the Cotati and Windsor basins near Santa Rosa) and regions with deep soft material but relatively fast Vs30 values (e.g., the region immediately east of the Hayward fault between Hayward and Richmond) may exceed that predicted by the NGA relations. This arises from the strong correlation between Vs30 and basin depth for the sites recording ground motions used to construct the NGA relations.

Our ground motion simulations include a reduction of the coseismic slip in creeping regions through either a slip-predictable approach or a vertical gradient in slip in the creeping regions. Both of these approaches reduce the earthquake magnitude for a given rupture area. Consideration of the end-member cases for the vertical-gradient approach (creep having no affect on coseismic slip and creep preventing any slip in creeping regions) demonstrates that considering creep when computing ground motions for Hayward fault scenario earthquakes reduces the amplitude of the ground motions compared to when creep is neglected. In the extreme case of no coseismic slip in creeping regions, the ground motions in Livermore and San Jose are about 50% smaller as a result of reduced excitation of surfaces waves associated with the limited amount of shallow slip. This highlights the important role of continued and improved characterization of the spatial extent and rates of creep along the Hayward fault for accurate assessment of the seismic hazard associated with the Hayward fault.

Digital Data Available

Modified Mercalli Intensities on uniform latitude and longitude grids along with velocity waveforms are available as USGS Data Series DS-??. For the Oakland and Alum Rock earthquakes the data series includes synthetic velocity waveforms at the stations shown in the electronic supplement. For the scenario earthquakes, the data series includes the MMI values on uniform grids and velocity waveforms at about 1000 sites for each scenario run by the modelers.

Data and Resources

Observed ground motions for the 2007 Mw 5.45 Alum Rock and 2007 Mw 4.18 Oakland earthquakes can be obtained from the IRIS Data Management Center at www.iris.edu (last accessed October 2009) and the USGS National Strong Motion Program at nsmp.wr.usgs.gov (last accessed October 2009). The USGS Bay Area Velocity Model 08.3.0 can be obtained from www.sf06simulation.org (last accessed October 2009). All other data used in this paper

came from published sources listed in the references. Many of the figures were generated using Generic Mapping tools (Wessel and Smith, 1998) and the low-pass filtering of the waveforms was performed using SAC2000 (Goldstein *et al*., 2003).

Acknowledgments

In analyzing the ground motions we benefited from discussions with Paul Spudich, David Boore, and Ken Campbell. We thank ?? and ?? for careful reviews of the manuscript. Aagaard, Brocher, Simpson, and Jachens were funded by the Earthquake Hazard Program of the U.S. Geological Survey. Graves and Ma were supported with funding from the Southern California Earthquake Center (SCEC). SCEC is funded by NSF Cooperative Agreement EAR-0529922 and USGS Cooperative Agreement 07HQAG0008. Rodgers, Petersson, and Larsen were supported with funding from the Department of Energy and was performed under the auspices of the U.S. Department of Energy by Lawrence Livermore National Laboratory under Contract DE-AC52-07NA27344. This is SCEC contribution number ?? and LLNL contribution LLNL-JRNL-XXXYYY.

References

Aagaard, B. T., T. M. Brocher, D. Dolenc, D. Dreger, R. W. Graves, S. Harmsen, S. Hartzell, S. Larsen, K. McCandless, S. Nilsson, N. A. Petersson, A. Rodgers, B. Sjögreen, and M. L. Zoback (2008, April). Ground motion modeling of the 1906 San Francisco earthquake II: Ground motion estimates for the 1906 earthquake and scenario events. *Bulletin of the Seismological Society of America 98*(2), 1012–1046.

Aagaard, B. T., T. M. Brocher, D. Dolenc, D. Dreger, R. W. Graves, S. Harmsen, S. Hartzell, S. Larsen, and M. L. Zoback (2008, April). Ground motion modeling of the 1906 San Francisco earthquake I: Validation using the 1989 Loma Prieta earthquake. *Bulletin of the Seismological Society of America 98*(2), 989–1011.

Aagaard, B. T., R. W. Graves, D. Schwartz, J. Linkaemper, D. A. Ponce, and R. W. Graymer (XXXX). Ground motion modeling of Hayward fault scenario earthquakes I: Construction of the suite of scenarios. in preparation.

Aagaard, B. T., J. F. Hall, and T. H. Heaton (2001, May). Characterization of near-source ground motions with earthquake simulations. *Earthquake Spectra 17*(2), 177–207.

Aagaard, B. T. and T. H. Heaton (2004, December). Near-source ground motions from simulations of sustained intersonic and supersonic fault rupture. *Bulletin of the Seismological Society of America 94*(6), 2064–2078.

Abrahamson, N. and W. Silva (2008, February). Summary of the Abrahamson & Silva NGA ground-motion relations. *Earthquake Spectra 24*(1), 67–97.

Anderson, J. G. (2000, December). *Kocaeli, Turkey, earthquake of August 17, 1999: Reconnaissance report*, Volume 16, Chapter 6: Implications for seismic hazard analysis, pp. 113–137. Earthquake Engineering Research Institute.

Anderson, J. G. and S. E. Hough (1984, October). A model for the shape of the fourier amplitude spectrum of acceleration at high frequencies. *Bulletin of the Seismological Society of America 74*(5), 1969–1993.

Appelö, D. and N. A. Petersson (2008). A stable finite difference method for the elastic wave equation on complex geometries with free surfaces. *Communications in Computational Physics 5*(1), 84–107.

Archuleta, R. J. (1984, June 10). A faulting model for the 1979 Imperial-Valley earthquake. *Journal of Geophysical Research - Solid Earth 89*(B6), 4559–4585.

Bakun, W. H. (1999). Seismic activity of the San Francisco Bay region. *Bulletin of the Seismological Society of America 89*(3), 764–784.

Boatwright, J. and H. Bundock (2008). Modified Mercalli Intensity maps for the 1868 Hayward earthquake plotted in ShakeMap format. Open-File Report 2008-1121, U.S. Geological Survey. http://pubs.usgs.gov/of/2008/1121/ (last accessed 2/18/2009).

Boore, D. M. (1983, December). Stochastic simulation of high-frequency ground motions based on seismological models of the radiated spectra. *Bulletin of the Seismological Society of America 73*(6A), 1865–1894.

Boore, D. M. and G. M. Aktinson (2008, February). Ground-motion prediction equations for the average horizontal component of PGA, PGV, and 5%-damped PSA at spectral periods between 0.01 s and 10.0 s. *Earthquake Spectra 24*(1), 99–138.

Boore, D. M. and W. B. Joyner (1997, April). Site amplifications for generic rock sites. *Bulletin of the Seismological Society of America 87*(2), 327–341.

Bouchon, M., M. P. Bouin, H. Karabulut, M. N. Toksoz, M. Dietrich, and A. J. Rosakis (2001, July 15). How fast is rupture during an earthquake? New insights from the 1999 Turkey earthquakes. *Geophysical Research Letters 28*(14), 2723–2726.

Bouchon, M., N. Toksoz, H. Karabulut, M. P. Bouin, M. Dietrich, M. Aktar, and M. Edie (2000, September 15). Seismic imaging of the 1999 Izmit (Turkey) rupture inferred from the near-fault recordings. *Geophysical Research Letters 27*(18), 3013–3016.

Bouchon, M. and M. Vallee (2003, August 8). Observation of long supershear rupture during the magnitude 8.1 Kunlunshan earthquake. *Science 301*(5634), 824–826.

Brocher, T. (2008, April). Compressional and shear-wave velocity versus depth relations for common rock types in northern California. *Bulletin of the Seismological Society of America 98*(2), 950–968.

Brocher, T. M., A. L. Ruebel, and E. E. Brabb (1997). Compilation of 59 sonic and density logs from 51 oil test wells in the San Francisco Bay area, California. Open-File Report 97-687, U.S. Geological Survey. http://geopubs.wr.usgs.gov/open-file/of97687/ (last accessed 4/27/2009).

Campbell, K. W. and Y. Bozorgnia (2008, February). NGA ground motion model for the geometric mean horizontal component of PGA, PGV, PGD and 5% damped linear elastic response spectra for periods ranging from 0.01 to 10 s. *Earthquake Spectra 24*(1), 139–171.

Chiou, B. S. and R. R. Youngs (2008, February). An NGA model for the average horizontal component of peak ground motion and response spectra. *Earthquake Spectra 24*(1), 173–215.

Day, S. M., R. Graves, J. Bielak, D. Dreger, S. Larsen, K. B. Olsen, A. Pitarka, and L. Ramirez-Guzman (2008, February). Model for basin effects on long-period response spectra in southern California. *Earthquake Spectra 24*(1), 257–277.

Dreger, D. and A. Kaverina (2000). Seismic remote sensing for the earthquake source process and nearsource strong shaking: A case study of the October 16, 1999 Hector Mine earthquake. *Geophysical Research Letters 27*(13), 1941–1944.

Dreger, D. S. and B. Romanowicz (1994). Source characteristics of events in the San Francisco Bay region. Open-File Report 94-176, U.S. Geological Survey.

Dunham, E. M. and R. J. Archuleta (2004, dec). Evidence for a supershear transient during the 2002 Denali earthquake. *Bulletin of the Seismological Society of America 68*(6B), S256–S268.

Ellsworth, W. L., M. Celebi, J. R. Evans, E. G. Jensen, M. C. Metz, D. J. Nyman, J. W. Roddick, P. Spudich, and C. D. Stephens (2004, August). Near-field ground motions of the M 7.9 November 3, 2002, Denali Fault, Alaska, earthquake recorded at pump station 10. *Earthquake Spectra 20*(3), 597–615.

Frankel, A. (1995, August). Simulating strong motions of large earthquakes using recordings of small earthquakes: the Loma Prieta mainshock as a test case. *Bulletin of the Seismological Society of America 85*(4), 1144–1160.

Goldstein, P., M. Dodge, D. Firpo, and L. Minner (2003). *The IASPEI International Handbook of Earthquake and Engineering Seismology*, Chapter SAC2000: Signal processing and analysis tools for seismologists and engineers. London: Academic Press.

Graves, R. W. (1996, August). Simulating seismic-wave propagation in 3-D elastic media using staggered-grid finite-differences. *Bulletin of the Seismological Society of America 86*(4), 1091–1106.

Graves, R. W., B. T. Aagaard, K. W. Hudnut, L. M. Star, J. P. Stewart, and T. H. Jordan (2008, November). Broadband simulations for Mw 7.8 southern San Andreas earthquakes: Ground motion sensitivity to rupture speed. *Geophysical Research Letters 35*(L22302).

Graves, R. W. and A. Pitarka (2004). Broadband time history simulation using a hybrid approach. In *13th World Conference on Earthquake Engineering Conference Proceedings*, Vancouver, Canada. paper no. 1098.

Graymer, R. W. (2000). *Geologic map and map database of the Oakland metropolitan area, Alameda, Contra Costa, and San Francisco Counties, California*. U.S. Geological Survey Map MF-2342. 1 sheet, scale 1:50,000, http://pubs.usgs.gov/mf/2000/2342/ (last accessed 2009/04/15).

Harmsen, S., S. Hartzell, and P. Liu (2008, June). Simulated ground motion in Santa Clara Valley, California, and vicinity from m$\geq$6.7 scenario earthquakes. *Bulletin of the Seismological Society of America 98*(3), 1243–1271.

Hartzell, S., S. Harmsen, A. Frankel, and S. Larsen (1999, December). Calculation of broadband time histories of ground motion: Comparison of methods and validation using strong-ground motion from the 1994 Northridge earthquake. *Bulletin of the Seismological Society of America 89*(6), 1484–1504.

Hartzell, S., S. Harmsen, R. A. Williams, D. Carver, A. Frankel, G. Choy, R. C. Jachens, T. M. Brocher, and C. M. Wentworth (2006, October). Modeling and validation of a 3D velocity structure for the Santa Clara Valley, California, for seismic-wave simulations. *Bulletin of the Seismological Society of America 96*(5), 1851–1881.

Kim, A., D. S. Dreger, and S. Larsen (XXXX). Moderate earthquake ground motion validation in the San Francisco Bay area. submitted to the Bulletin of the Seismological Society of America.

Larsen, S. and C. A. Schultz (1995). Elas3d: 2D/3D elastic finite-difference wave propagation code. Technical Report UCRL-MA-121792, Lawrence Livermore National Laboratory. 19 p.

Larsen, S. C., D. Dreger, M. Antolik, and C. Stidham (2000). 3-D simulations of scenario earthquake along the Hayward fault. Technical Report UCRL-ID-137645, Lawrence Livermore National Laboratory. 8 p.

Liu, P., R. J. Archuleta, and S. H. Hartzell (2006, December). Prediction of broadband ground-motion time histories: Hybrid low/high- frequency method with correlated random source parameters. *Bulletin of the Seismological Society of America 96*(6), 2118–2130.

Ma, S., R. J. Archuleta, and M. J. Page (2007, December). Effects of large-scale surface topography on ground motions, as demonstrated by a study of the San Gabriel Mountains, Los Angeles, California. *Bulletin of the Seismological Society of America 97*(6), 2066–2079.

Ma, S. and P. Liu (2006, October). Modeling of the perfectly matched layer absorbing boundaries and intrinsic attenuation in explicit finite-element methods. *Bulletin of the Seismological Society of America 96*(5), 1779–1794.

Ma, S., G. A. Prieto, and G. C. Beroza (2008, December). Testing community velocity models for Southern California using the ambient seismic field. *Bulletin of the Seismological Society of America 98*(6), 2694–2714.

Nilsson, S., N. A. Petersson, B. Sjögreen, and H. O. Kreiss (2007). Stable difference approximations for the elastic wave equation in second order formulation. *SIAM Journal on Numerical Analysis 45*(5), 1902–1936.

Olson, A. H. and R. J. Apsel (1982, December). Finite faults and inverse-theory with applications to the 1979 Imperial-
547 Valley earthquake. *Bulletin of the Seismological Society of America 72*(6), 1969–2001.

Pasyanos, M. E., D. Dreger, and B. Romanowicz (1996, October). Toward real-time estimation of regional moment
548 tensors. *Bulletin of the Seismological Society of America 86*(5), 1255–1269.

Rodgers, A., N. A. Petersson, S. Nilsson, B. Sjogreen, and K. McCandless (2008, April). Broadband waveform model-
ing of moderate earthquakes in the San Francisco Bay Area and preliminary assessment of the USGS 3-D seismic
549 velocity model. *Bulletin of the Seismological Society of America 98*(2), 969–988.

Rowshandel, B. (XXXX). Fault rupture directivity effects in the next generation attenuation relations. submitted to
550 Earthquake Spectra.

Seekins, L. and J. Boatwright (2007). Rupture directions for selected northern California earthquakes.
551 http://earthquake.usgs.gov/regional/nca/rupture/. last accessed November, 2009.

Sekiguchi, H. and T. Iwata (2002, February). Rupture process of the 1999 Kocaeli, Turkey, earthquake estimated from
552 strong-motion waveforms. *Bulletin of the Seismological Society of America 92*(1), 300–311.

Somerville, P. G., K. Irikura, R. Graves, S. Sawada, D. Wald, N. Abrahamson, Y. Iwasaki, T. Kagawa, N. Smith, and
A. Kowada (1999, January/February). Characterizing crustal earthquake slip models for the prediction of strong
553 ground motion. *Seismological Research Letters 70*(1), 199–222.

Somerville, P. G., N. F. Smith, R. W. Graves, and N. A. Abrahamson (1997, January/February). Modification of
empirical strong ground motion attenuation relations to include the amplitude and duration effects of rupture
554 directivity. *Seismological Research Letters 68*(1), 199–222.

Spudich, P. and B. S. J. Chiou (2008, February). Directivity in NGA earthquake ground motions: Analysis using
555 isochrone theory. *Earthquake Spectra 24*(1), 279–298.

Spudich, P. and E. Cranswick (1984, December). Direct observation of rupture propagation during the 1979 Impe-
rial Valley earthquake using a short baseline accelerometer array. *Bulletin of the Seismological Society of Amer-*
556 *ica 74*(6), 2083–2114.

Stover, C. W. and J. L. Coffman (1993). Seismicity of the United States, 1568–1989 (revised). Professional Paper
557 1527, U.S. Geological Survey.

Thurber, C. H., T. M. Brocher, H. Zhang, and V. E. Langenheim (2007). Three-dimensional P wave velocity model for
558 the San Francisco Bay region, California. *Journal of Geophysical Research - Solid Earth 112*(B07313).

Walling, M., W. Silva, and N. Abrahamson (2008, February). Nonlinear site amplification factors for constraining the
559 nga models. *Earthquake Spectra 24*(1), 243–255.

Wessel, P. and W. H. F. Smith (1998). New, improved version of the generic mapping tools released. *EOS Transactions 79*, 579.

Williams, A. J., T. M. Brocher, W. D. Mooney, and A. Boken (1999). Data report for seismic refraction surveys conducted from 1980 to 1982 in the Livermore Valley and the Santa Cruz mountains, California. Open-File Report 99-146, U.S. Geological Survey. http://geopubs.wr.usgs.gov/open-file/of99-146/ (last accessed 4/27/2009).

Wills, C. J., M. Petersen, W. A. Bryant, M. Reichle, G. J. Saucedo, S. Tan, G. Taylor, and J. Treiman (2000, December). A site-conditions map for California based on geology and shear-wave velocity. *Bulletin of the Seismological Society of America 90*(6B), S187–S208.

Working Group on California Earthquake Probabilities (2003). Earthquake probabilities in the San Francisco Bay region: 2002–2031. Open-File Report 03-214, U.S. Geological Survey.

Working Group on California Earthquake Probabilities (2008). The uniform California earthquake rupture forecast, version 2 (UCERF 2). Open-File Report 2007-1437, U.S. Geological Survey. http://pubs.usgs.gov/of/2007/1437/ (last accessed 2/18/2009).

Yu, E. and P. Segall (1996). Slip in the 1868 Hayward earthquake from the analysis of historical triangulation data. *Journal of Geophysical Research - Solid Earth 101*(B7), 16101–16118.

U.S. Geological Survey, MS977

345 Middlefield Rd.

Menlo Park, CA 94025

(B.T.A., T.M.B., R.W.S.)

URS Corporation

566 El Dorado St.

Pasadena, CA 91101

(R.W.G.)

Deptartment of Geol. Sciences

San Diego State University

5500 Campanile Dr.

San Diego, CA 92182-1020

(S.M.)

Lawrence Livermore National Laboratory
Box 808, L-103
Livermore, CA 94551-0808
(S.C.L.)

Center for the Study of Imaging and Dynamics of the Earth
University of California, Santa Cruz
Santa Cruz, CA 95064
and Lawrence Livermore National Laboratory
7000 East Ave, L-046
Livermore, CA 94551
(A.R.)

Center for Applied Scientific Computing
Computations Directorate
Lawrence Livermore National Laboratory
Box 808, L-422
Livermore, CA 94551-0808
(N.A.P.)

U.S. Geological Survey, MS989
345 Middlefield Rd.
Menlo Park, CA 94025
(R.J.)

Seismological Laboratory
University of California, Berkeley
215 McCone Hall
Berkeley, CA 94720
(D.D.)

612

Table 1. Wave Propagation Codes and Modeling Domains

	Aagaard	Graves	Larsen	Ma	Rodgers & Petersson
Domain					
Length	210 km	220 km	220 km	200 km	200 km
Width	126 km	280 km	150 km	120 km	120 km
Max. depth	40 km	45 km	45 km	36 km	40 km
NW corner	-123.4900, 38.2106	-123.6806, 38.1748	-123.5538, 38.3068	-123.4900, 38.2100	-123.3592, 38.1664
NE corner	-122.3313, 38.8890	-121.6198, 39.3223	-122.1802, 39.0988	-122.3800, 38.8500	-122.2500, 38.8000
SE corner	-120.9265, 37.3568	-119.9391, 37.3956	-120.7000, 37.5000	-121.0300, 37.4000	-120.9216, 37.3465
SW corner	-122.0742, 36.6920	-121.9729, 36.2774	-122.0669, 36.7080	-122.1400, 36.7600	-122.0206, 36.7129
Projection	transverse Mercator	oblique Mercator	spheroidal	spheroidal	spheroidal
Discretization	unstructured FE	staggered-grid FD	staggered-grid FD	structured FE	node-centered FD
Space	2nd order	4th order	4th order	2nd order	2nd order
Time	2nd order	2nd order	2nd order	2nd order	2nd order
Resolution	variable	125 m	100 m	variable	100 m
Bandwidth	$T > 2.0$ s	$T > 1.0$ s	$T > 1.0$ s	$T > 2.0$ s	$T > 2.0$ s
Min. Vs	700 m/s	620 m/s	500 m/s	500 m/s	500 m/s
Features					
Topography	yes	"squashed"	yes	yes	yes
Water	air filled	N/A	included	air filled	air filled
Mat. Properties	USGS 08.3.0	USGS 08.3.0	USGS 08.3.0	USGS 08.3.0	USGS 08.3.0
Attenuation	no	Graves	USGS VM08.3.0	no	no
Eq source	offset in mesh	point sources	point sources	point sources	point sources
# pt. sources	N/A	31,460	31,460	31,460	10,500
Fault surface	3-D geologic model	3-D geologic model	3-D geologic model	3-D geologic model	3-D geologic model

The corners of the bounding boxes of each domain are given in longitude and latitude (WGS84 horizontal datum).

Table 2. Earthquake Scenarios

Name	Rupture Segments	Slip Distribution	Hypocenter	Rupture Speed	Rise Time	Moment Magnitude	Modeling Groups
HS G01 HypoO	HS	G01	Oakland	*Vr92*	*Tr15*	6.76	A,G,L,M,R
HS G01 HypoH	HS	G01	Hayward	*Vr92*	*Tr15*	6.76	A,G,L,M,R
HS G01 HypoF	HS	G01	Fremont	*Vr92*	*Tr15*	6.76	A,G,L,M,R
HS G02 HypoO	HS	G02	Oakland	*Vr92*	*Tr15*	6.76	A
HS G02 HypoH	HS	G02	Hayward	*Vr92*	*Tr15*	6.76	A
HS G02 HypoF	HS	G02	Fremont	*Vr92*	*Tr15*	6.76	A
HS P01 HypoO	HS	P01	Oakland	*Vr92*	*Tr15*	6.84	A
HS P01 HypoH	HS	P01	Hayward	*Vr92*	*Tr15*	6.84	A
HS P01 HypoF	HS	P01	Fremont	*Vr92*	*Tr15*	6.84	A
HS+HN G04 HypoSPB	HS+HN	G04	San Pablo Bay	*Vr92*	*Tr15*	7.05	A,G,L,R
HS+HN G04 HypoO	HS+HN	G04	Oakland	*Vr92*	*Tr15*	7.05	A,G,L,M,R
HS+HN G04 HypoF	HS+HN	G04	Fremont	*Vr92*	*Tr15*	7.05	A,G,L,R
HS+HN P03 HypoSPB	HS+HN	P03	San Pablo Bay	*Vr92*	*Tr15*	6.97	A
HS+HN P03 HypoO	HS+HN	P03	Oakland	*Vr92*	*Tr15*	6.97	A
HS+HN P03 HypoF	HS+HN	P03	Fremont	*Vr92*	*Tr15*	6.97	A
CC+HS G03 HypoO	CC+HS	G03	Oakland	*Vr92*	*Tr15*	6.90	A
CC+HS G03 HypoH	CC+HS	G03	Hayward	*Vr92*	*Tr15*	6.90	A
CC+HS G03 HypoAR	CC+HS	G03	Alum rock	*Vr92*	*Tr15*	6.90	A
CC+HS P02 HypoO	CC+HS	P02	Oakland	*Vr92*	*Tr15*	6.94	A
CC+HS P02 HypoH	CC+HS	P02	Hayward	*Vr92*	*Tr15*	6.94	A
CC+HS P02 HypoAR	CC+HS	P02	Alum Rock	*Vr92*	*Tr15*	6.94	A
HN+RC G05 HypoSPB	HN+RC	G05	San Pablo Bay	*Vr92*	*Tr15*	6.89	A
HN+RC P04 HypoSPB	HN+RC	P04	San Pablo Bay	*Vr92*	*Tr15*	7.11	A
HS+HN+RC G06 HypoSPB	HS+HN+RC	G06	San Pablo Bay	*Vr92*	*Tr15*	7.16	A
HS+HN+RC P05 HypoSPB	HS+HN+RC	P05	San Pablo Bay	*Vr92*	*Tr15*	7.20	A
HS Vr82	HS	*G01*	*Hayward*	Vr82	*Tr15*	6.76	M
HS Vr141	HS	*G01*	*Hayward*	Vr141	*Tr15*	6.76	M
HS+HN Vr82	HS+HN	*G04*	*Oakland*	Vr82	*Tr15*	7.05	M
HS+HN Vr141	HS+HN	*G04*	*Oakland*	Vr141	*Tr15*	7.05	M
HS Tr10	HS	*G01*	*Hayward*	*Vr92*	Tr10	6.76	L
HS Tr20	HS	*G01*	*Hayward*	*Vr92*	Tr20	6.76	L
HS Tr10u	HS	*G01*	*Hayward*	*Vr92*	Tr10u	6.76	L
HS+HN Tr10	HS+HN	*G04*	*Oakland*	*Vr92*	Tr10	7.05	L
HS+HN Tr20	HS+HN	*G04*	*Oakland*	*Vr92*	Tr20	7.05	L
HS+HN Tr20u	HS+HN	*G04*	*Oakland*	*Vr92*	Tr20u	7.05	L
HS N01	HS	N01	*Hayward*	*Vr92*	*Tr15*	6.89	A
HS F01	HS	F01	*Hayward*	*Vr92*	*Tr15*	6.61	A
HS+HN N04	HS+HN	N04	*Oakland*	*Vr92*	*Tr15*	7.12	A
HS+HN F04	HS+HN	F04	*Oakland*	*Vr92*	*Tr15*	6.82	A

Figure 5 shows the rupture lengths and epicenters. The rise time labels Tr10, Tr15, and Tr20 correspond to values of 1.0, 1.5, and 2.0 for C in the expression for the rise time, $t_{95}/t_0 = C\sqrt{D_f/D_0}$, and the labels Tr10u and Tr20u correspond to nominally uniform rise times of 1.0 s and 2.0 s. The rupture speed labels Vr92, Vr82, and Vr141 correspond to the correlations between rupture speed and slip. The maximum local rupture speeds for Vr92, Vr82, and Vr141 are 0.92 Vs, 0.82 Vs, and $\sqrt{2}$ Vs, respectively. The modeling groups are Aagaard (A), Graves (G), Larsen (L), Ma (M), and Rodgers and Petersson (R). We form the scenario names from abbreviations of the parameters but do not include parameters with significant redundancy (which are shown in italics).

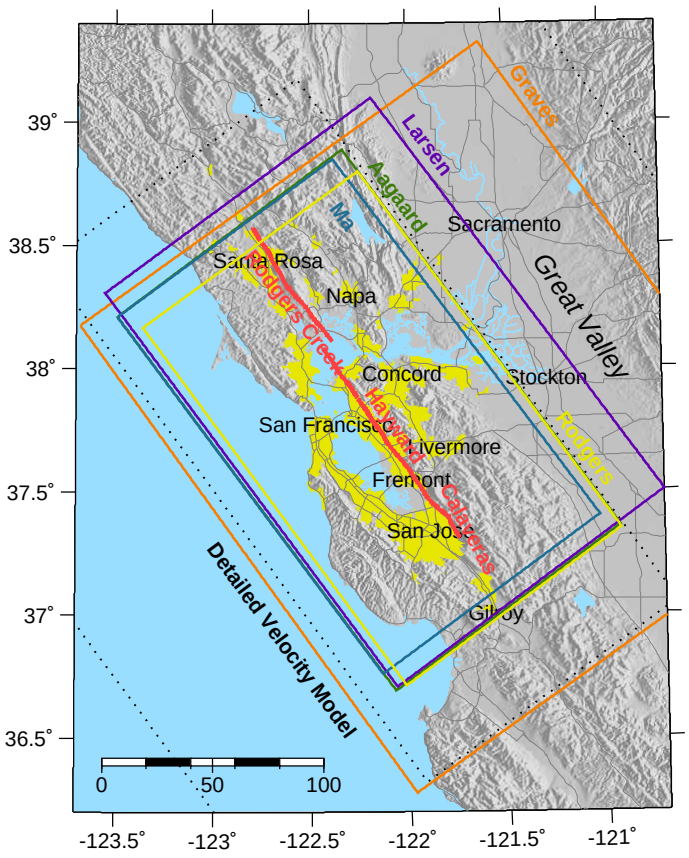

Figure 1. Bounding boxes of the domains (colored boxes) used by the five ground-motion modeling groups and the detailed and regional portions of the USGS Bay Area Velocity Model 08.3.0. (dotted black boxes). The red lines show the extent of rupture on the surface traces in our scenario earthquakes on the Hayward, Rodgers Creek, and Calaveras faults. The shaded yellow region delineates the San Francisco Bay urban area.

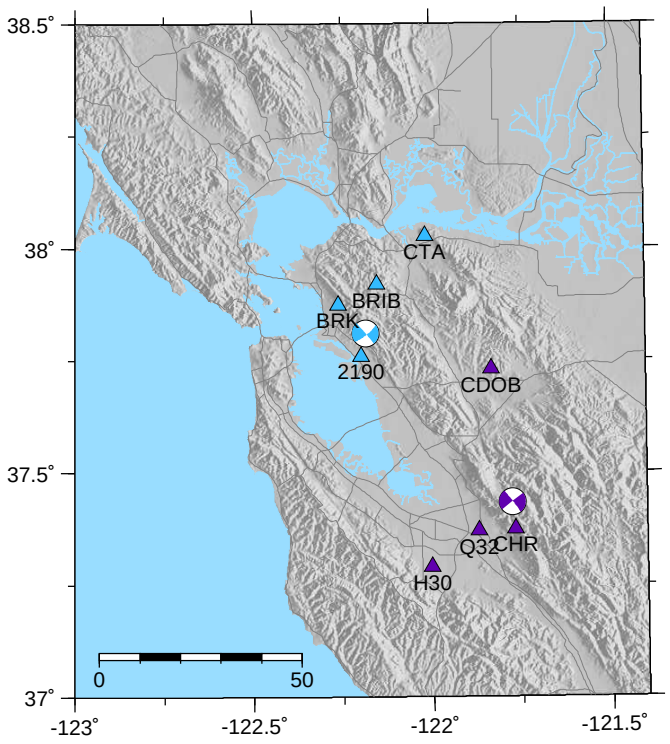

Figure 2. Map of the San Francisco Bay Area showing the double couple focal mechanisms for the two moderate earthquakes we modeled for validation: 2007/10/31 Alum Rock (Mw 5.45) and 2007/07/20 Oakland (Mw 4.18). Also shown are seismic stations (triangles, color coded by event) used for waveform comparisons.

630

631

632

633

634

635

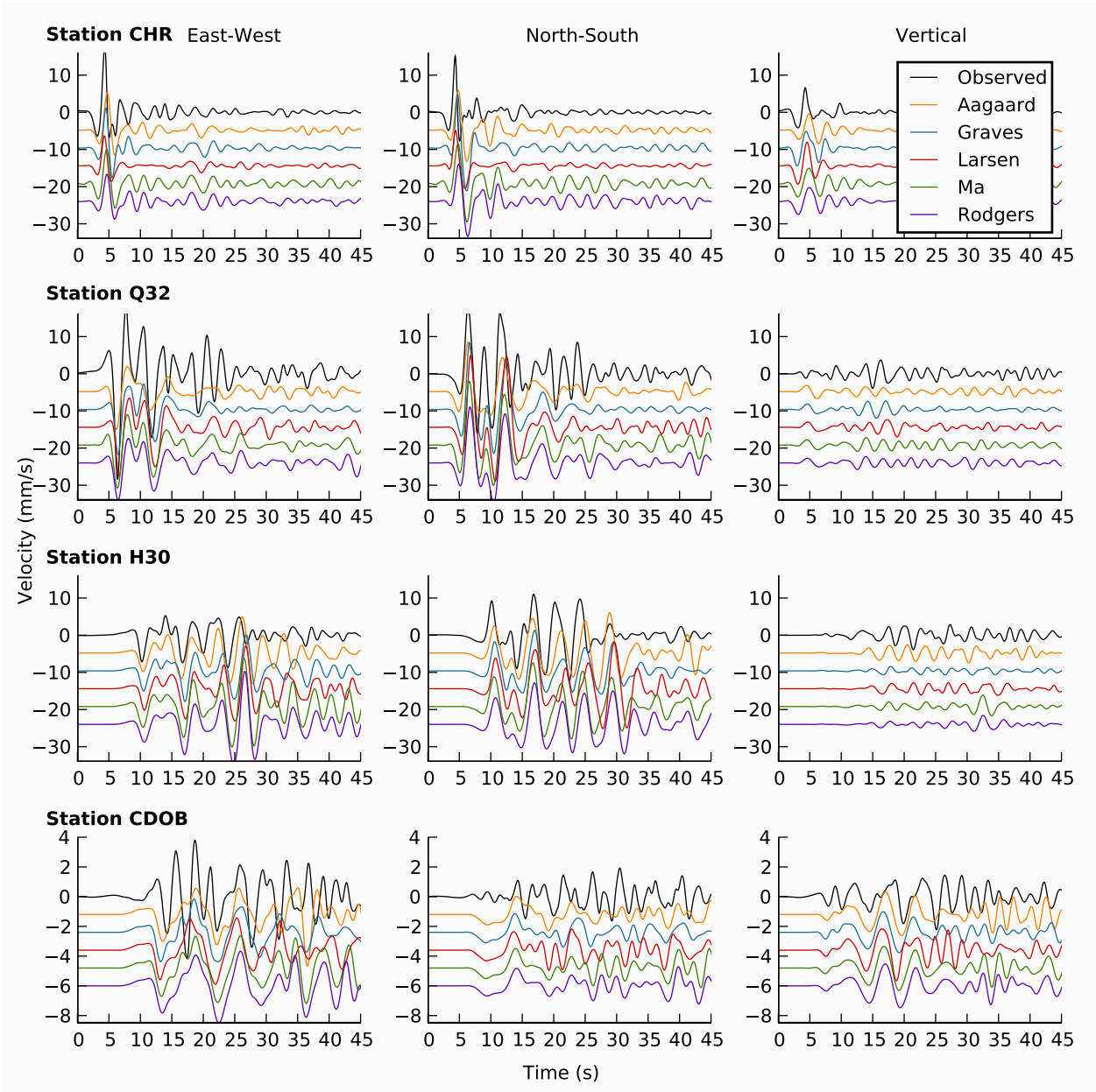

Figure 3. Observed (black) and simulated (color-coded by modeling group) velocity waveforms at four stations in the San Francisco Bay area for the 2007/10/31 Alum Rock earthquake. The velocity waveforms have been low-pass filtered to a common bandwidth of $T > 2.0$ s using two passes of a two-pole Butterworth filter with a corner frequency of 0.5 Hz.

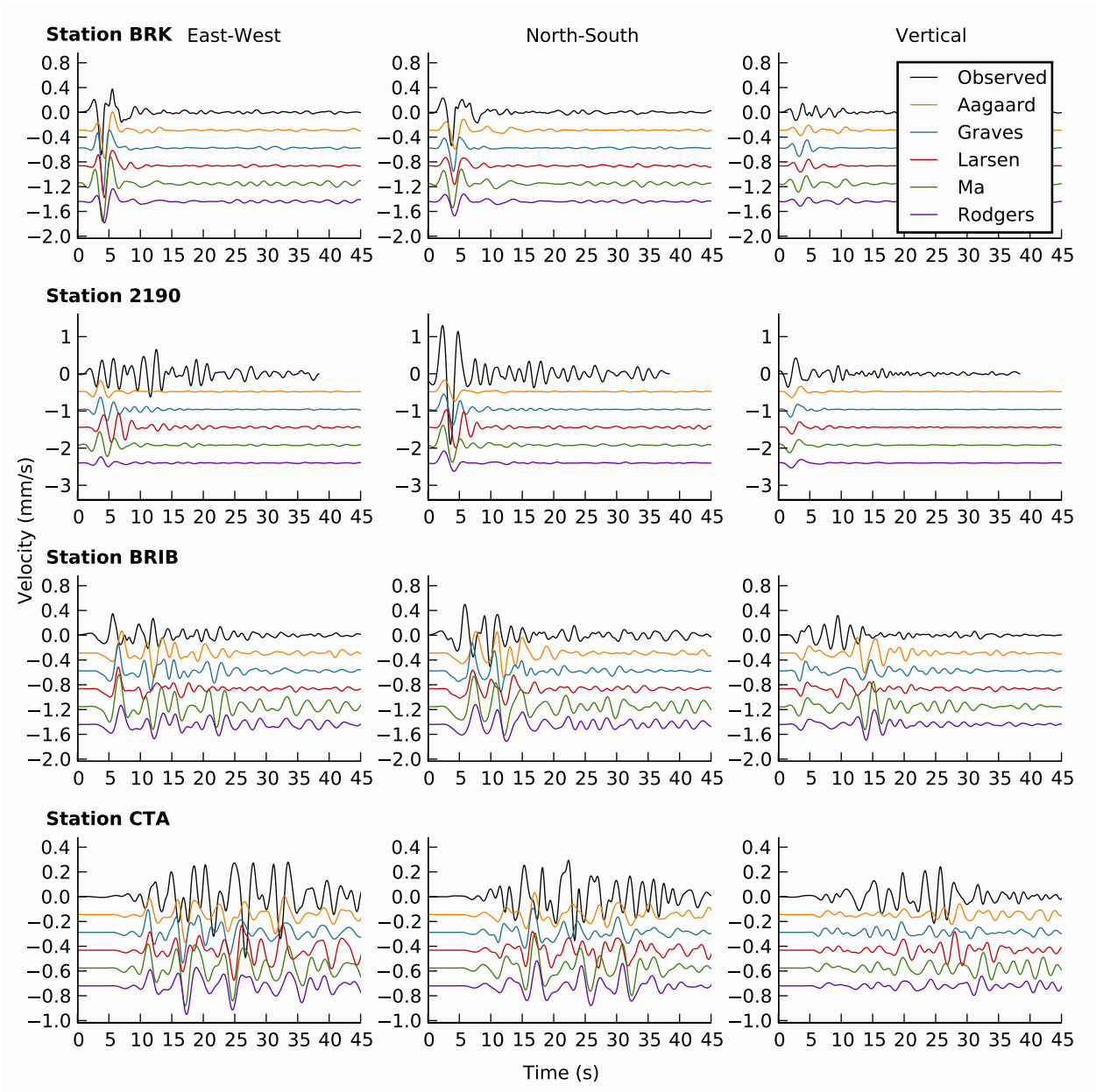

Figure 4. Observed (black) and simulated (color-coded by modeling group) velocity waveforms at four stations in the San Francisco Bay area for the 2007/07/20 Oakland earthquake. The velocity waveforms have been low-pass filtered to a common bandwidth of T $>$ 2.0 s using two passes of a two-pole Butterworth filter with a corner frequency of 0.5 Hz.

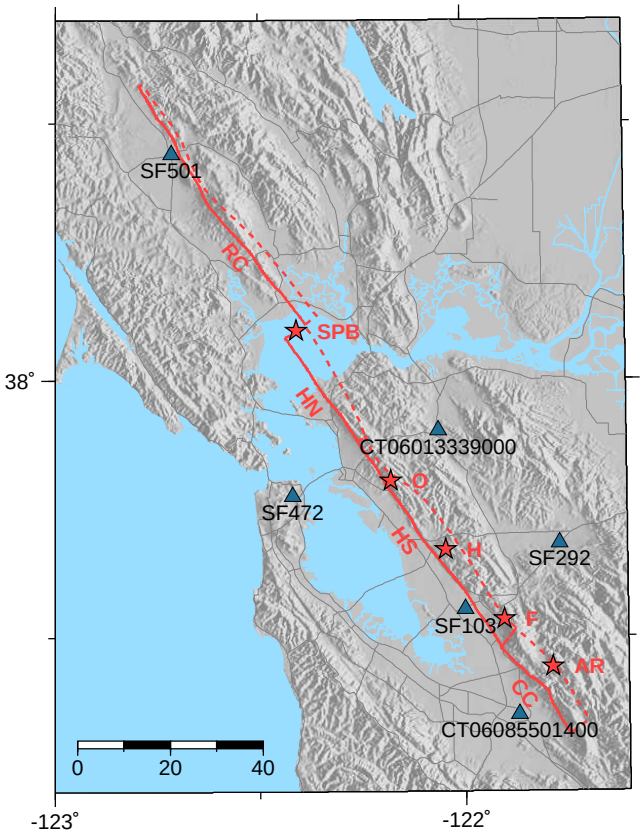

Figure 5. Rupture segments (surfaces traces in solid lines and down-dip extent of rupture in dashed lines) which are combined into the five rupture lengths. The epicenters (stars) are offset from the surface trace due to the 3-D geometry of the fault surface. The rupture segments include the Central Calaveras (CC), Hayward South (HS), Hayward North (HN), and Rodgers Creek (RC). The epicenters include San Pablo Bay (SPB), Oakland (O), Hayward (H), Fremont (F), and Alum Rock (AR).

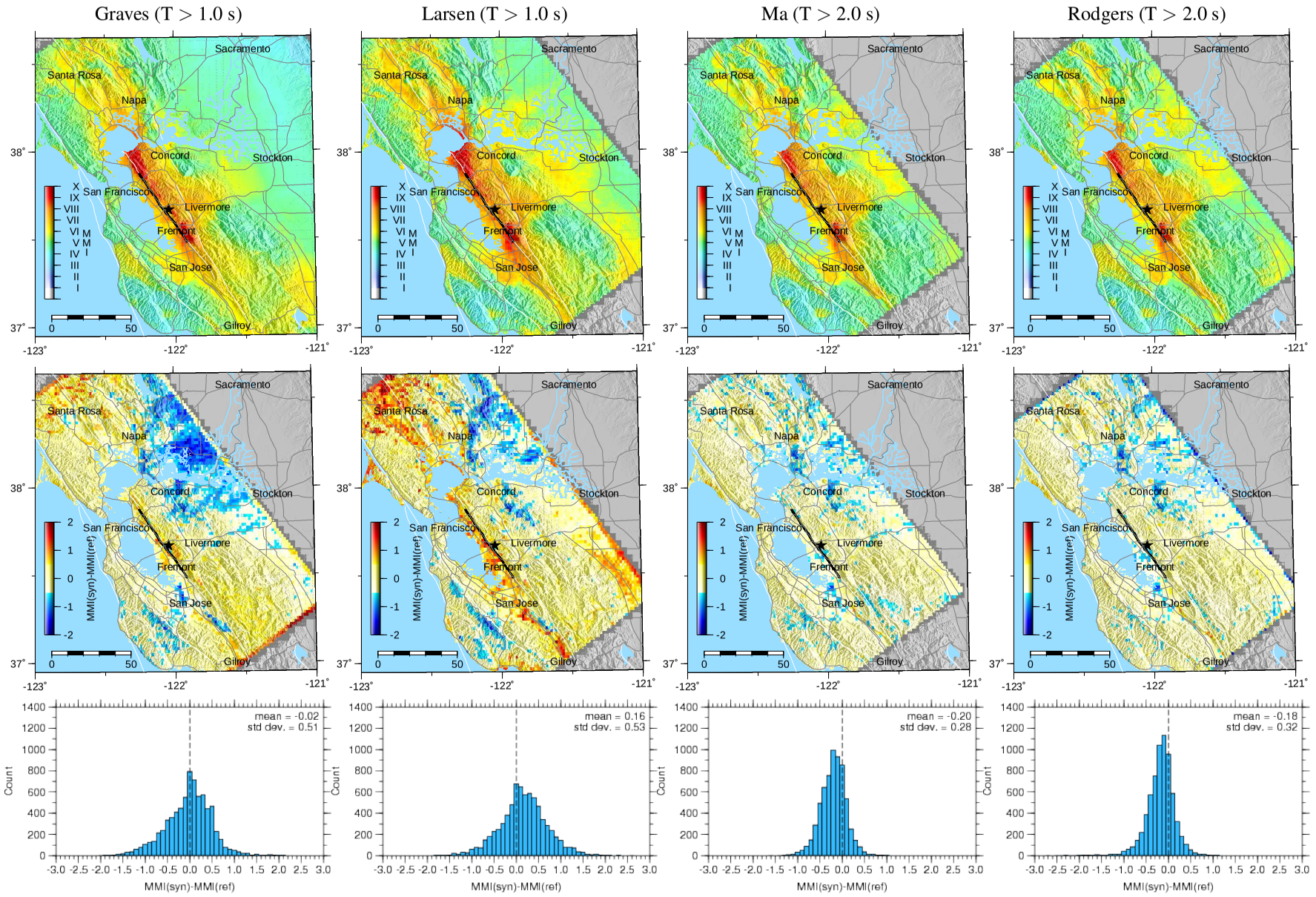

Figure 6. Comparison of Modified Mercalli Intensity (MMI) across the modeling groups for scenario HS G01 HypoH. The lower two rows show the residuals with respect Aagaard's MMI values (see Figure 8). The black line indicates the rupture and the black star identifies the epicenter. Aagaard, Ma, and Rodgers use the same minimum period and similar minimum shear wave speeds without intrinsic attenuation, resulting in very small residuals. Larsen and Graves include shorter periods and intrinsic attenuation, resulting in lower amplitudes in the Great Valley.

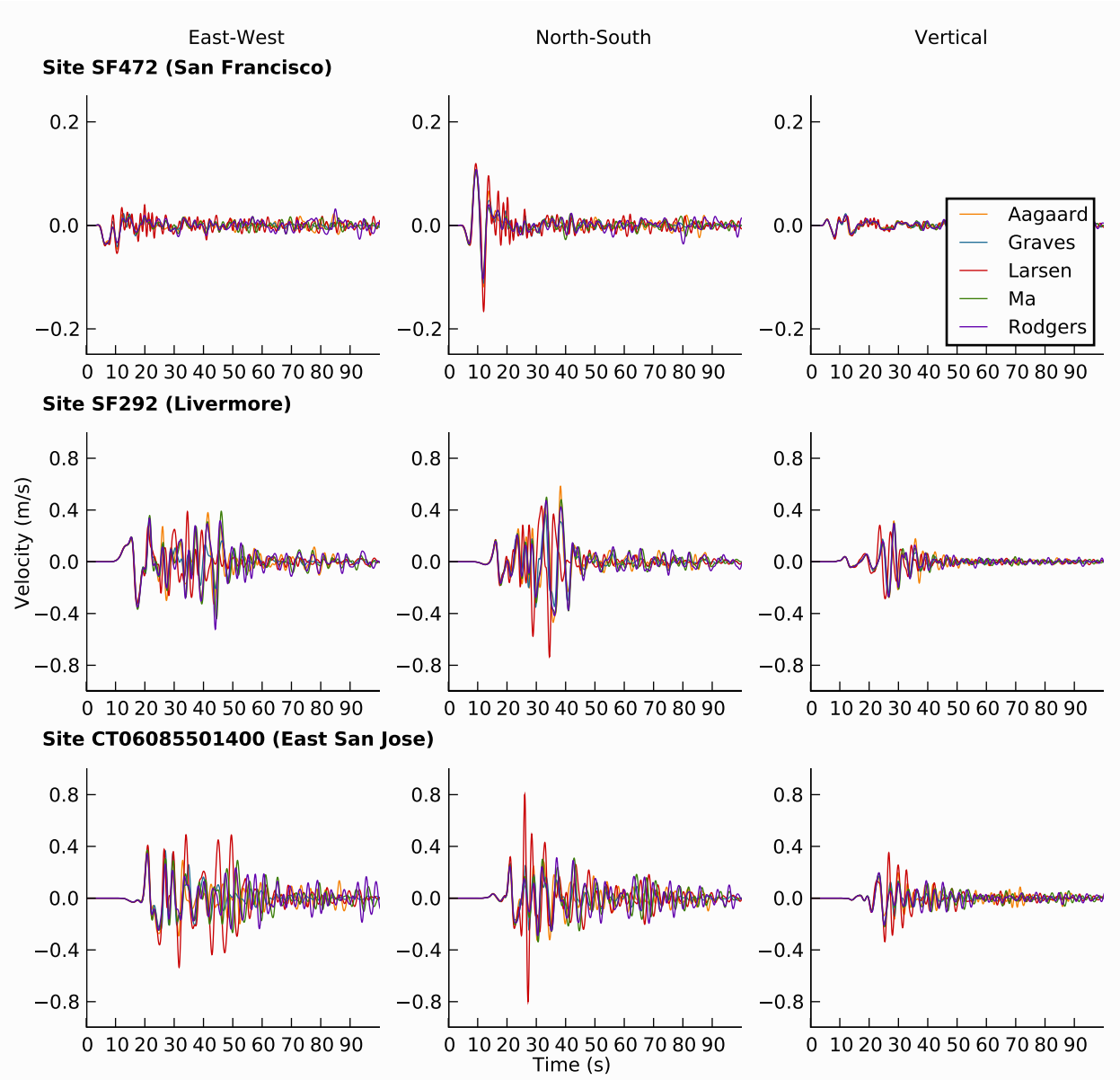

Figure 7. Long-period (T $>$ 2.0 s) velocity waveforms at three sites (see Figure 5) for scenario HS G01 HypoH for each of the five modeling groups. The waveforms demonstrate consistency in the amplitude and duration of shaking with nearly identical initial arrivals and some secondary arrivals.

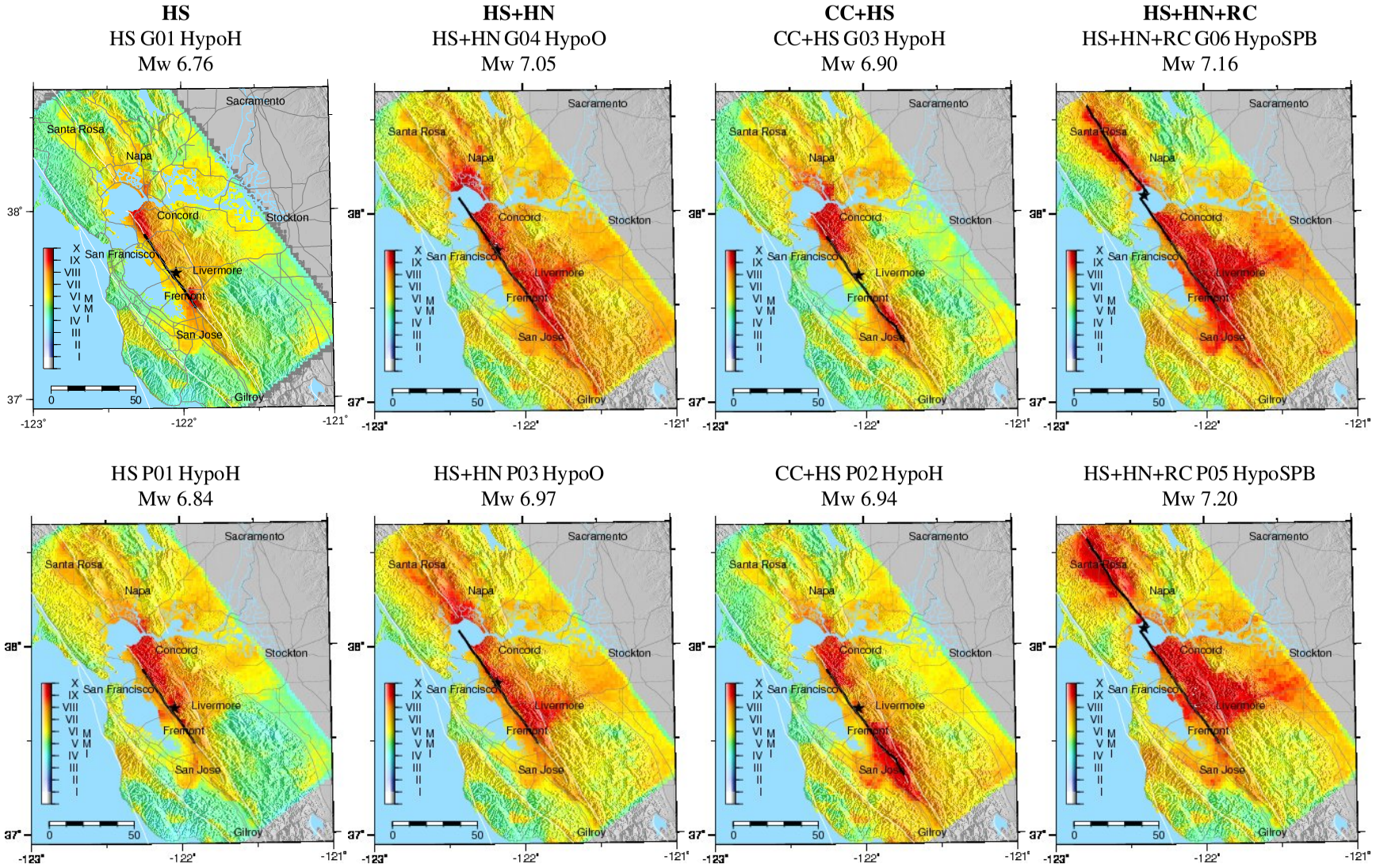

Figure 8. Modified Mercalli Intensities from Aagaard's long-period (T > 2.0 s) simulations of eight scenario earthquakes with different rupture lengths and slip distributions. Top row uses the slip-gradient approach for accounting for the effects of creep on the slip distribution, and the bottom row uses the slip-predictable approach. The black line indicates the rupture and the black star identifies the epicenter.

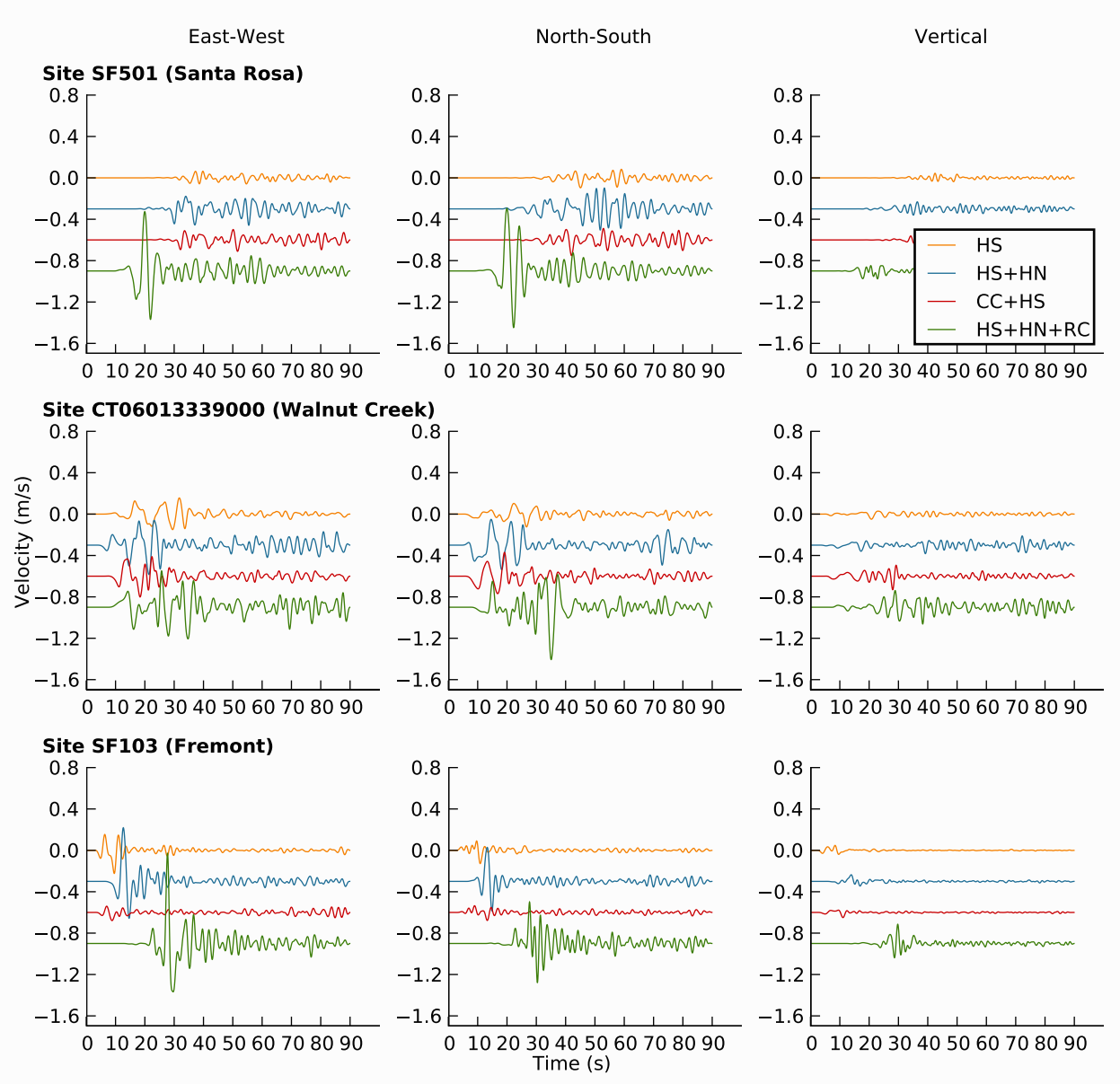

Figure 9. Velocity waveforms from Aagaard's long-period (T > 2.0 s) simulations of four scenario earthquakes with different rupture lengths and slip distributions. The scenarios are identified by their rupture lengths and include HS G01 HypoH (Mw 6.76), HS+HN G04 HypoO (Mw 7.05), CC+HS G03 HypoH (Mw 6.90), and HS+HN+RC G05 HypoSPB (Mw 7.16).

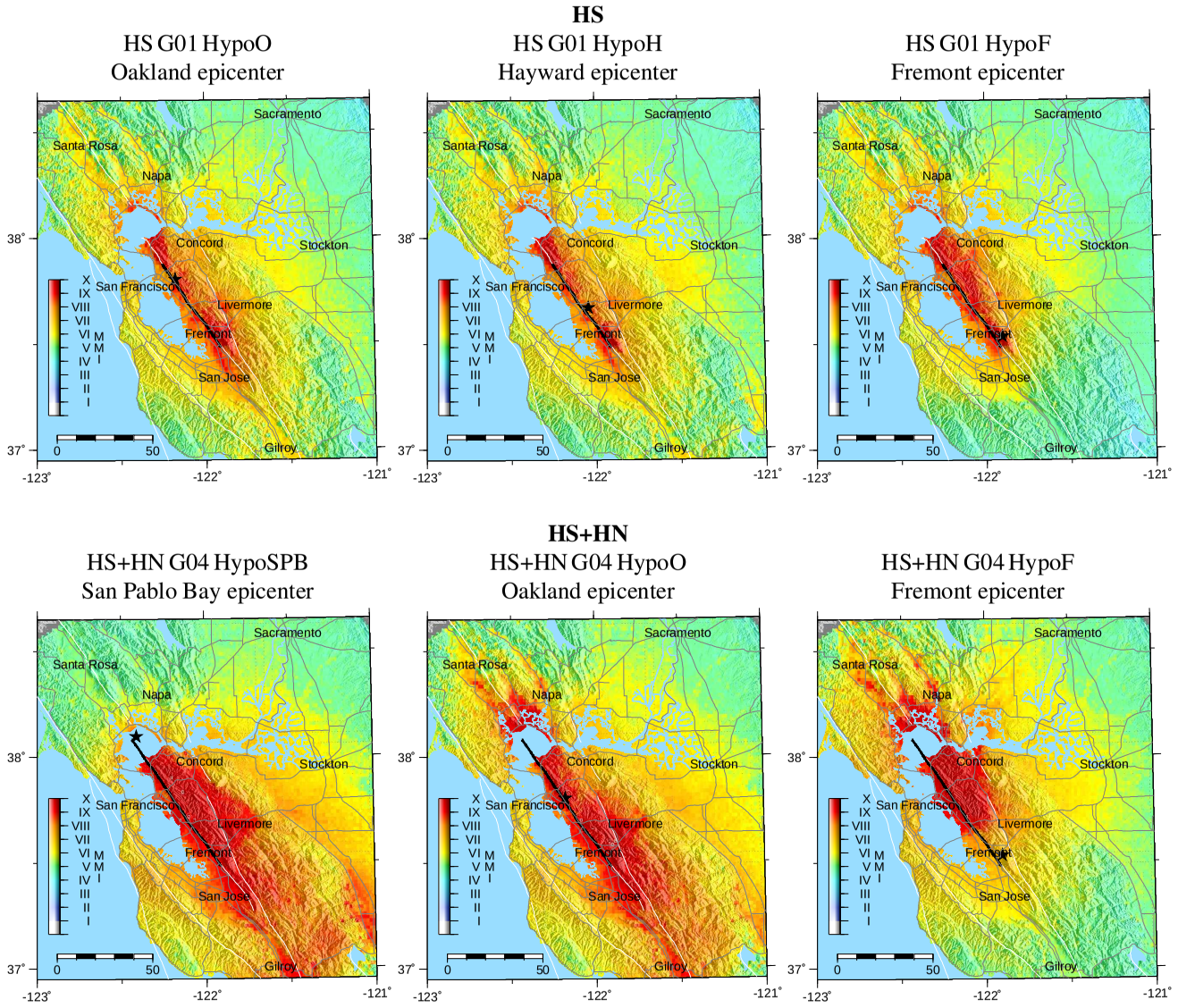

Figure 10. Modified Mercalli Intensities from Graves's broadband (T > 0.1 s) simulations of six scenario earthquakes with different hypocenters for the Hayward South rupture length (top row) and the Hayward South + North rupture length (bottom row). The black line indicates the rupture and the black star identifies the epicenter. Changing the hypocenter has a strong impact on the distribution of shaking by altering the rupture directivity.

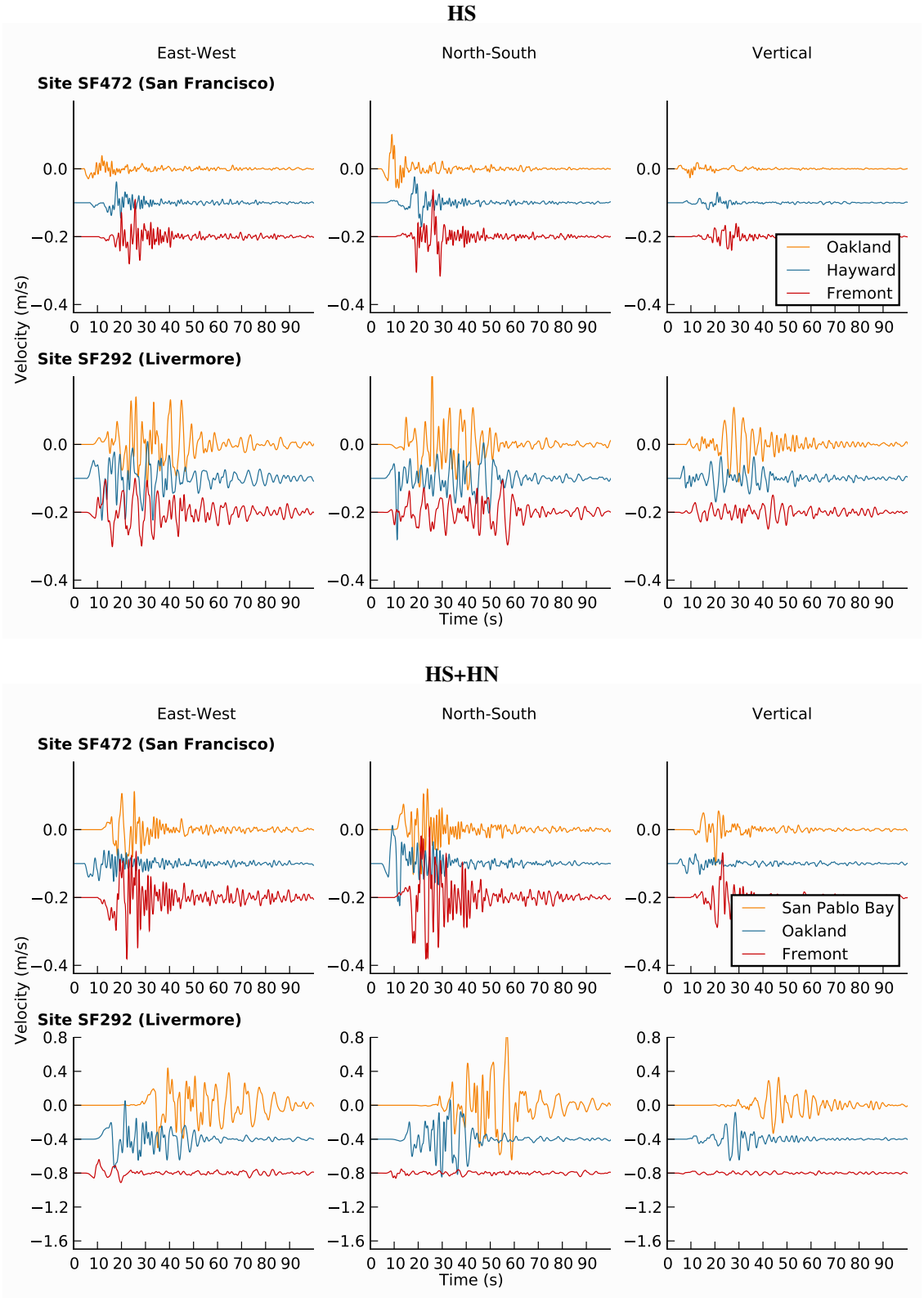

Figure 11. Velocity waveforms from Graves's broadband (T > 0.1 s) simulations of six scenario earthquakes with different hypocenters. The top two rows show waveforms for the Hayward South rupture length (scenarios HS G01 HypoO, Oakland epicenter; HS G01 HypoH, Hayward epicenter; and HS G01 HypoF, Fremont epicenter) and the bottom two rows show waveforms for the Hayward South + North rupture length (scenarios HS+HN G04 HypoSPB, San Pablo Bay epicenter; HS+HN G04 HypoO, Oakland epicenter; and HS+HN G04 HypoF, Fremont epicenter).

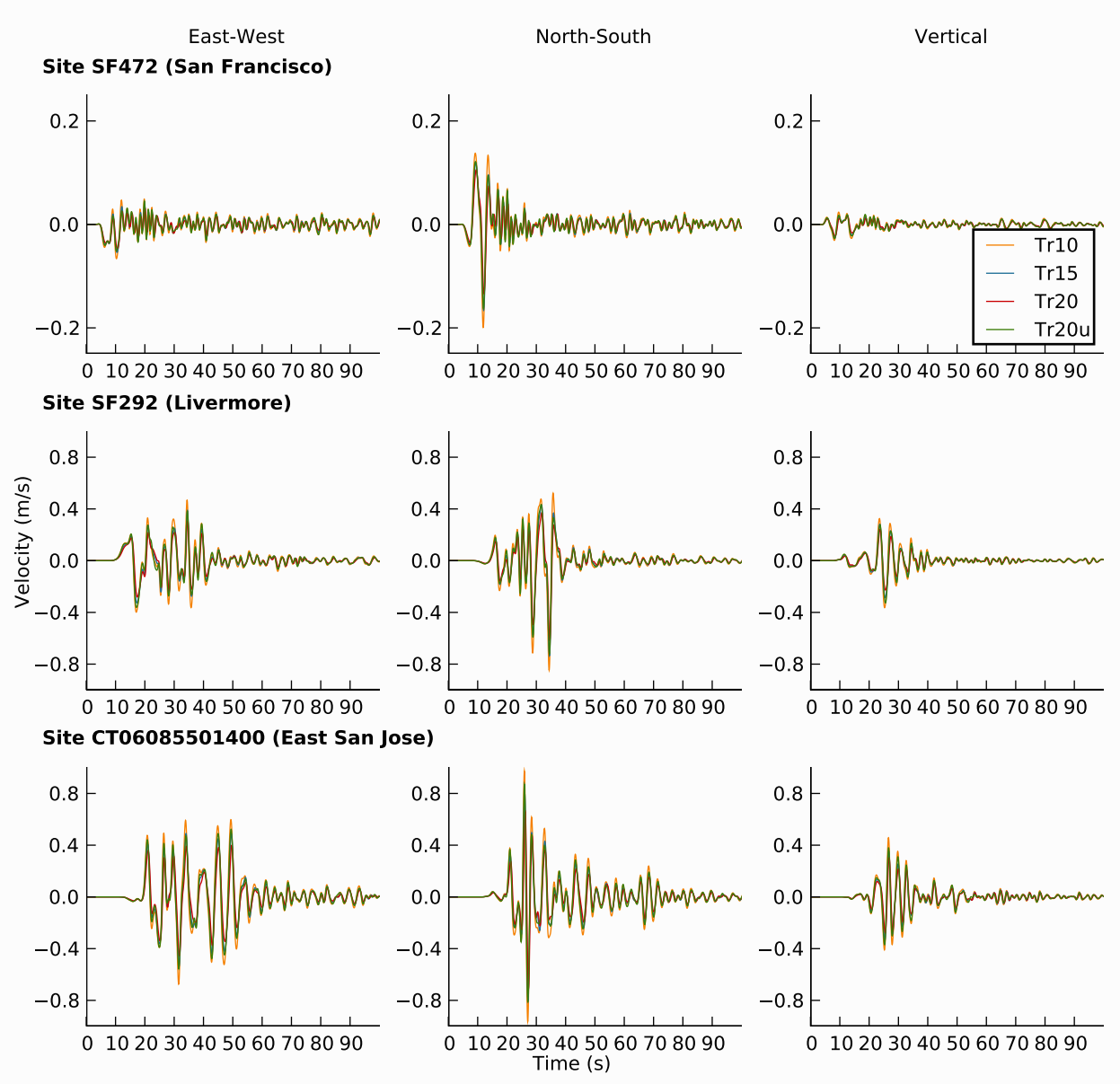

Figure 12. Velocity waveforms from Larsen's long-period (T $>$ 1.0 s) simulations of four scenario earthquakes with different rise time distributions. The scenarios are identified by the rise time and include HS+HN Tr10, HS+HN G04 HypoO (Tr15), HS+HN Tr20, and HS+HN Tr20u. The ground motions exhibit a relatively weak sensitivity to the variation in the rise time distribution.

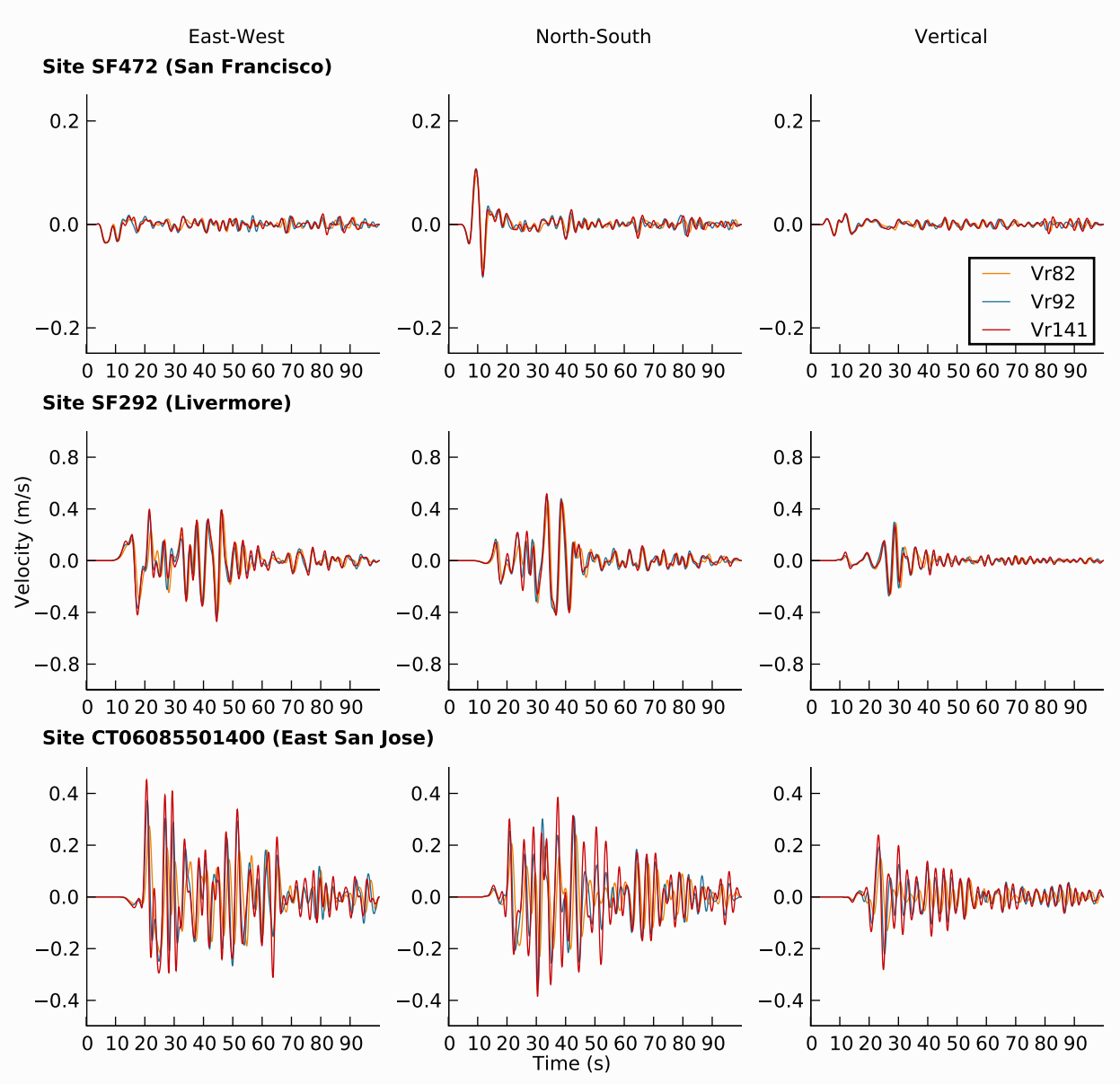

Figure 13. Velocity waveforms from Ma's long-period (T $>$ 2.0 s) simulations of three scenario earthquakes with different rupture speed distributions. The scenarios are identified by the rupture speed and include HS+HN Vr82, HS+HN G04 HypoO (Vr92), and HS+HN Vr141. The ground motions exhibit a relatively weak sensitivity to the variation in the rupture speed distribution.

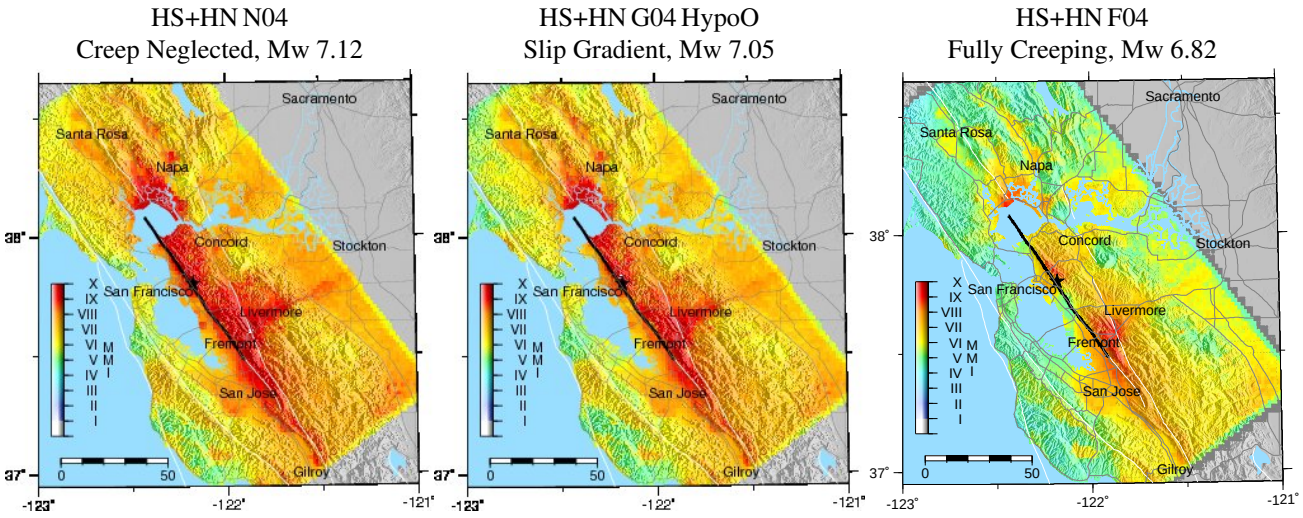

Figure 14. Modified Mercalli Intensities from Aagaard's long-period (T $>$ 2.0 s) simulations of three scenario earthquakes with different vertical gradients in the slip distribution in creeping regions. Scenario HS+HN N04 uses to a vertical gradient of 0 (neglecting creep), scenario HS+HN G04 HypoO uses a vertical gradient of -0.12 m/km, and scenario HS+HN F04 uses an infinite vertical gradient (preventing coseismic slip in creeping regions). The black line indicates the rupture and the black star identifies the epicenter. Creep reduces the coseismic slip in creeping regions, which lowers the magnitude and decreases the efficiency of radiating surface waves.

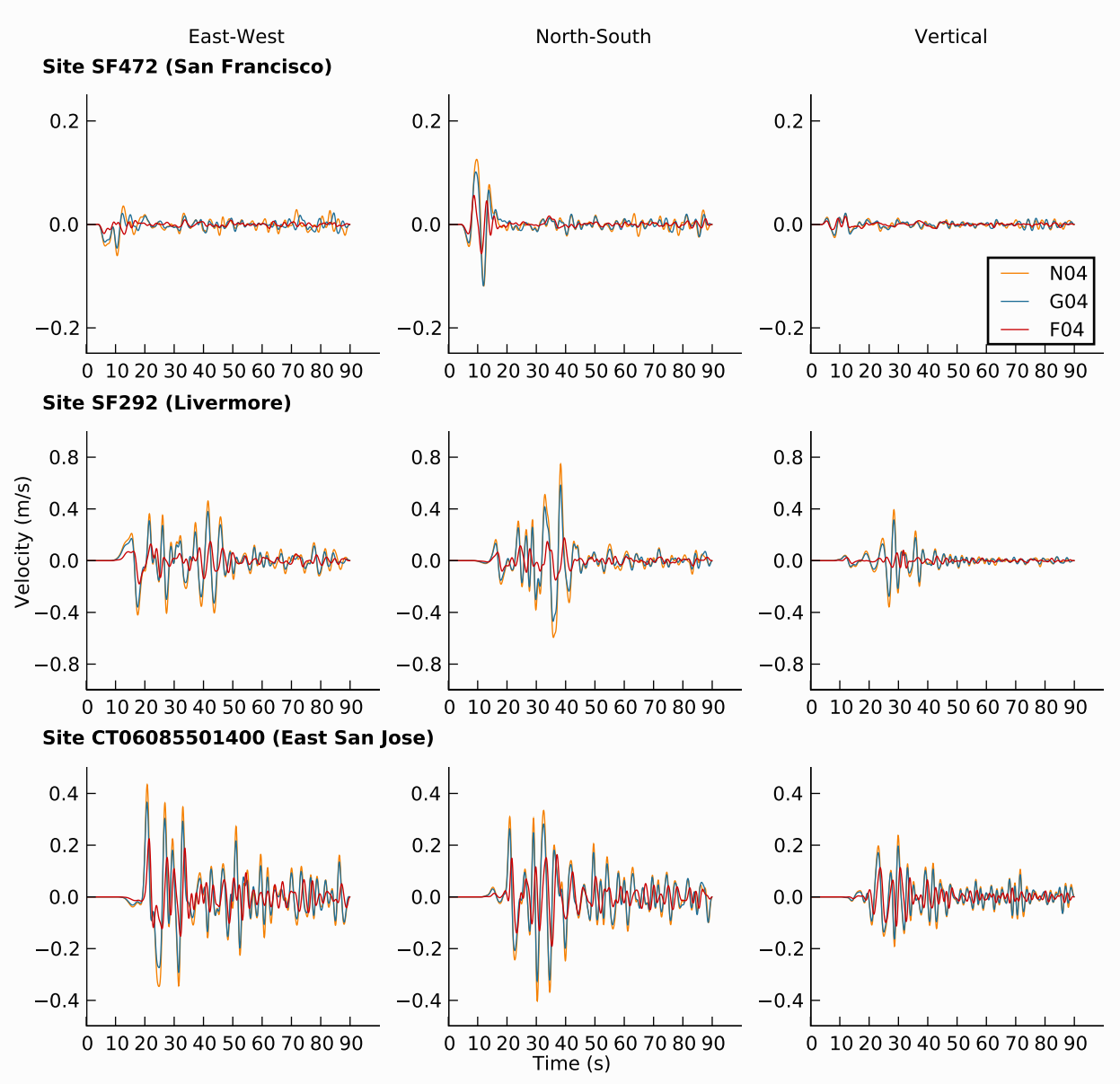

Figure 15. Velocity waveforms from Aagaard's long-period (T > 2.0 s) simulations of three scenario earthquakes with different vertical gradients in the slip distribution in creeping regions. The scenarios are identified by the slip distributions and include HS+HN N04, HS+HN G04 HypoO, and HS+HN F04. Creep reduces the coseismic slip in creeping regions, which lowers the magnitude and decreases the efficiency of radiating surface waves.

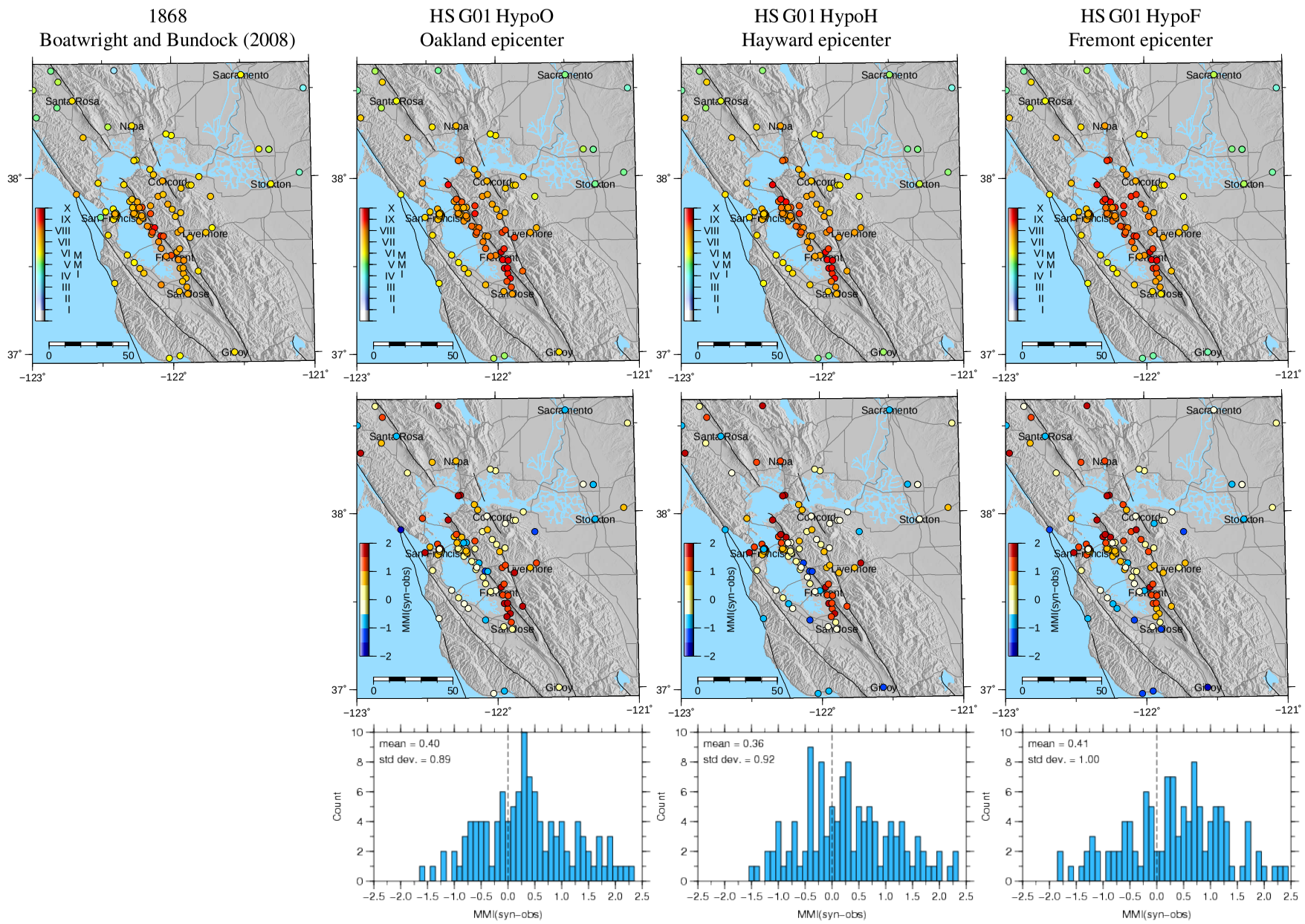

Figure 16. Comparison of MMI from Graves's broadband simulations of Hayward South scenario earthquakes with Boatwright and Bundock's compilation from the 1868 earthquake with the residuals for the synthetics shown in the bottom two rows. The bilateral rupture gives the lowest mean residual.

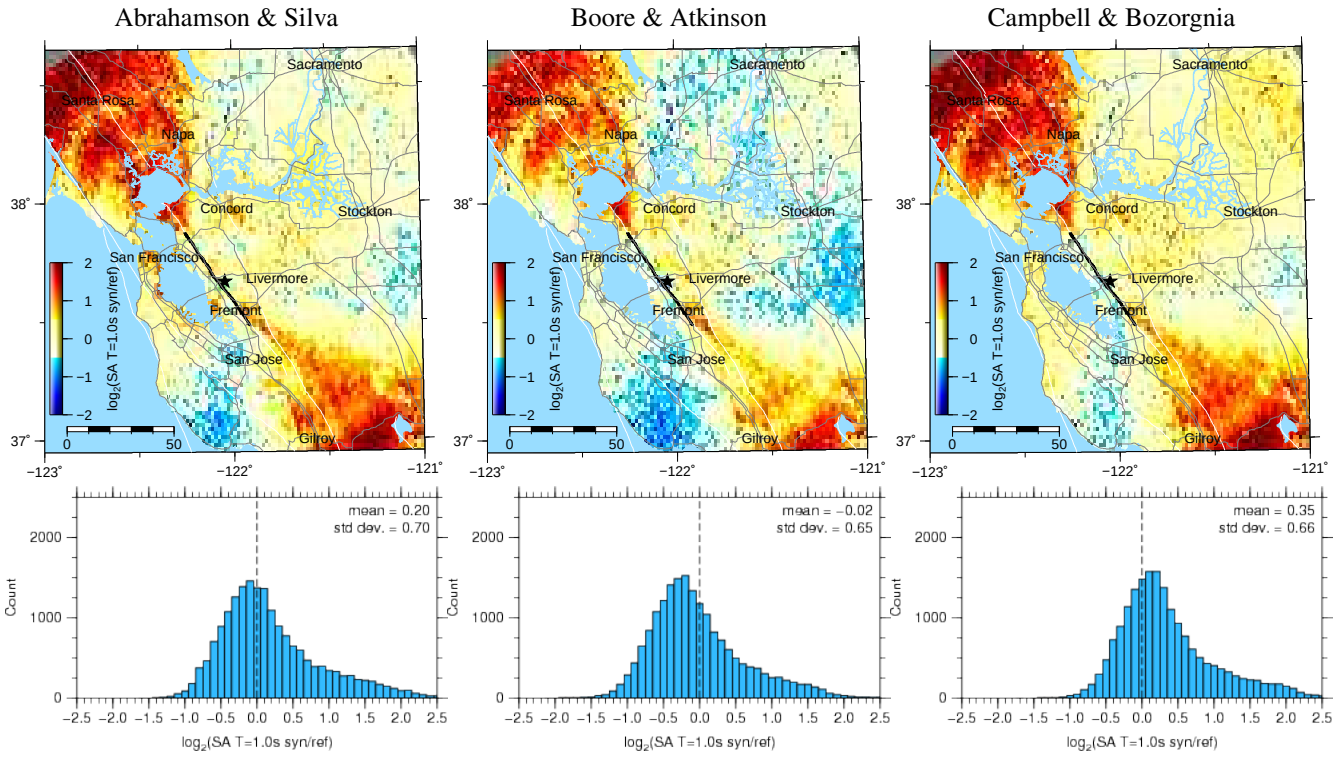

Figure 17. Comparison of spectral acceleration (SA) at 1.0 s from Graves's broadband ($T > 0.1$ s) simulation of scenario HS G01 HypoH with the Abrahamson and Silva, Boore and Atkinson, and Campbell and Bozorgnia NGA ground-motion prediction equations. Residuals are low along the length of the rupture and perpendicular to the fault. The simulation predicts higher spectral accelerations off the ends of the rupture due to rupture directivity, which is not explicitly included in the NGA models.

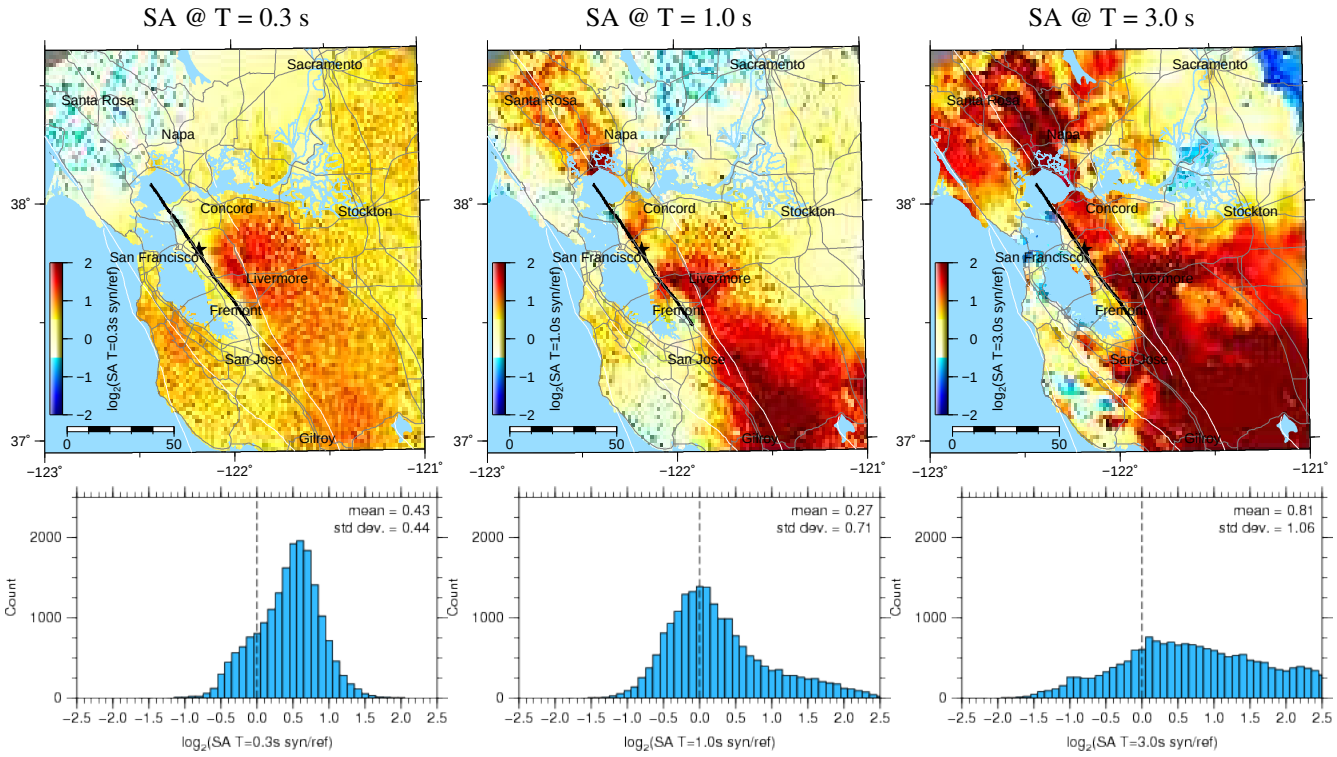

Figure 18. Comparison of spectral acceleration at 0.3 s, 1.0 s, and 3.0 s from Graves's broadband ($T > 0.1$ s) simulation of scenario HS+HN G04 HypoO with the Boore and Atkinson NGA ground-motion prediction equations. Residuals are generally low along the length of the rupture and perpendicular to the fault. The simulation predicts higher spectral accelerations off the ends of the rupture due to rupture directivity, especially at periods of 1.0 s and longer. The NGA models do not explicitly include directivity effects.

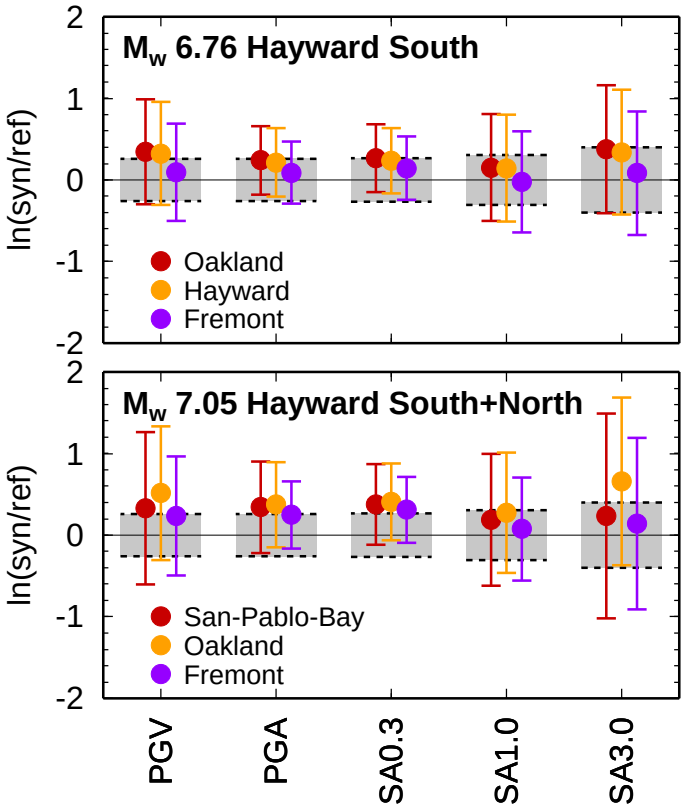

Figure 19. Summary of of the mean residuals and variances for Graves's six broadband (T $>$ 0.1 s) simulations of six scenario earthquakes averaged across the Abrahamson and Silva, Boore and Atkinson, and Campbell and Bozorgnia NGA ground-motion prediction equations. The gray shaded regions indicate the one standard deviation inter-event variability in the NGA relations. The mean residuals are within one standard deviation in most cases, indicating strong consistency between the 3-D ground-motion synthetics and the NGA relations.

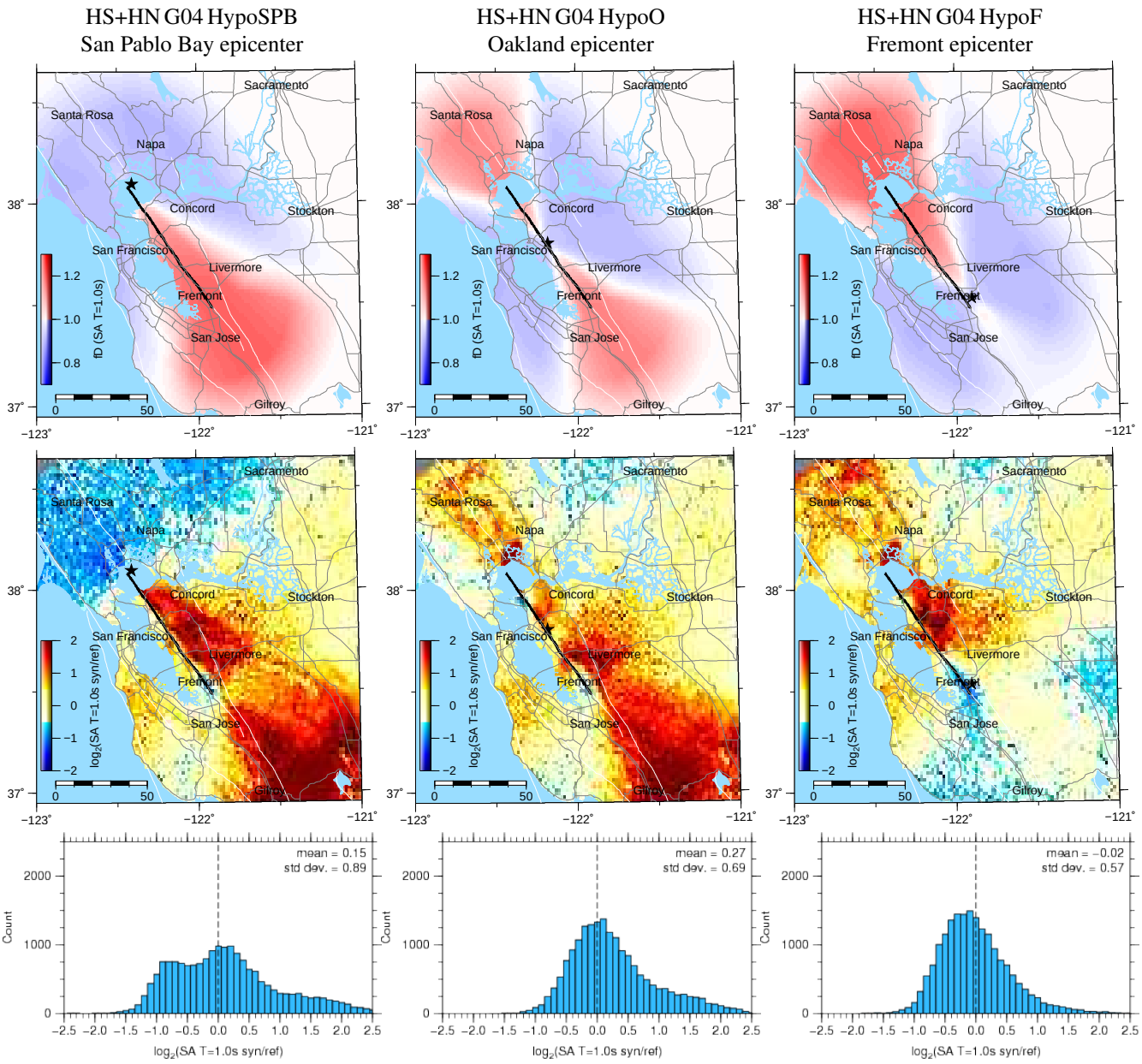

Figure 20. Comparison of spectral acceleration at 1.0 s from Graves's broadband ($T > 0.1$ s) simulations of scenario earthquakes with the Boore and Atkinson NGA ground-motion prediction equations (bottom two rows) adjusted by the Spudich-Chiou directivity correction (shown in the top row). The black line indicates the rupture and the black star identifies the epicenter. The directivity correction leads to a slight decrease in the standard deviation of the residuals. The 3-D simulations predict stronger directivity and extend it to greater distances than that predicted by the Spudich-Chiou directivity model.

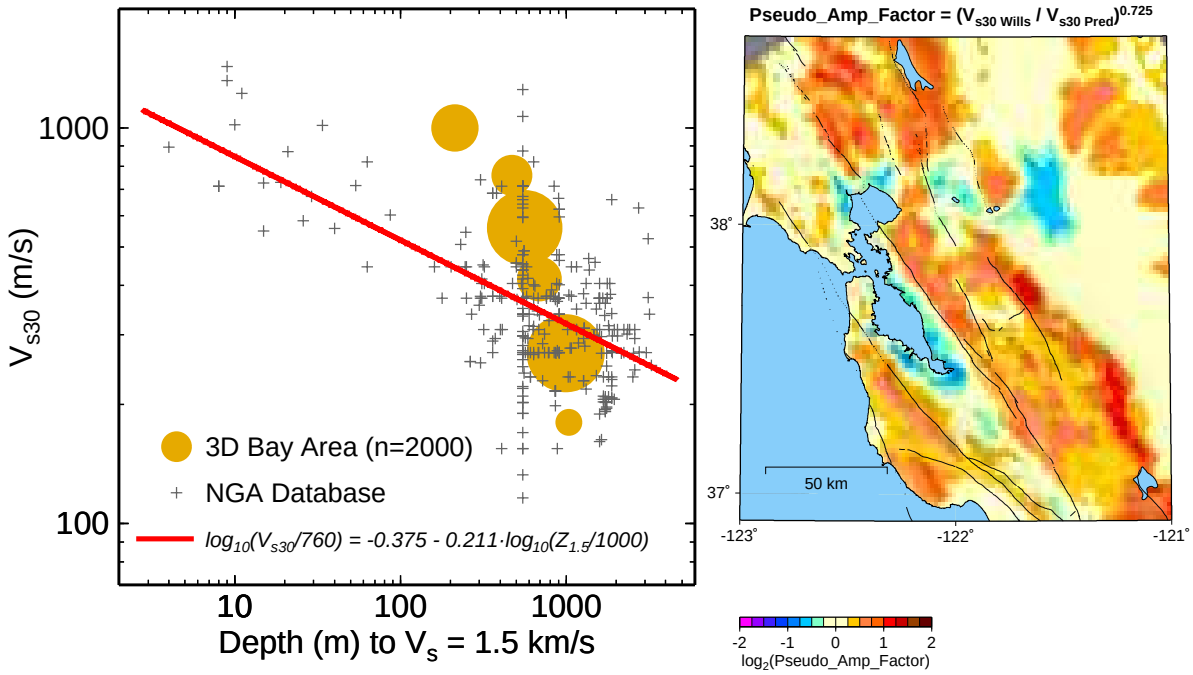

Figure 21. The left panel compares the correlation between Vs30 and depth to the 1.5 km/s isosurface in the San Francisco Bay area with sites in the NGA ground-motion database. Sites in the San Francisco Bay area do not exhibit the same correlation as those in the NGA database. The right panel shows a map of the amplification correction factor that attempts to capture the potential differences in spectral amplitude predicted by the Boore and Atkinson NGA model with those expected based on the depth to the Vs 1.5 km/s isosurface.